EFFECT OF ADDITIVE-MANUFACTURED FUEL GRAIN GEOMETRY ON SMALL-SCALE HYBRID ROCKET PERFORMANCE

By

ZACKERY JAMES BYCKO

Bachelor of Science in Aerospace Engineering
Oklahoma State University
Stillwater, Oklahoma
2021

Bachelor of Science in Mechanical Engineering
Oklahoma State University
Stillwater, Oklahoma
2021

Submitted to the Faculty of the
Graduate College of the
Oklahoma State University
in partial fulfillment of
the requirements for
the Degree of
MASTER OF SCIENCE
May, 2023

EFFECT OF ADDITIVE-MANUFACTURED FUEL GRAIN GEOMETRY ON SMALL-SCALE HYBRID ROCKET PERFORMANCE

Thesis Approved:

Dr. Kurt Rouser

Thesis Advisor

Dr. Sandip Harimkar

Dr. Khaled Sallam

ACKNOWLEDGMENTS

I would like to thank my advisor, Dr. Kurt Rouser, and committee members, Dr. Sandip Harimkar and Dr. Khaled Sallam, for accompanying me on this journey of scholarship and discovery. Additionally, I would like to thank my fellow graduate and undergraduate researchers past and present, including but not limited to Tanner Price, Chris Rathman, Andrew Walsh, Josh Anderson, Michael Patman, Soham Bhakta, and Katie Rupert for their willingness to aid over the course of this study.

I would like to thank my parents, Witek and Sharon Bycko, for their unwavering love and support throughout my life and education. The principles you both instilled in me have helped guide me along this path towards success. I will never be able to repay the sacrifices you have made to allow me to succeed. I would like to thank my older brother, Kaz Bycko, for setting such a notable example and showing me what hard work, determination, and resilience can accomplish.

Thank you to my friends Kaden Mendenhall, Tanner Kliewer, Destin Ortiz, Garrett Russell, John Thompson, and Jared Jeffers, for being a great support system and providing a comforting and nonjudgmental place to share my thoughts.

Lastly, I would like to thank Madison Noble for always encouraging me to be myself. Your unconditional love and support have supplied me with the confidence and stability necessary to become the best version of me. Thank you for pushing me to relentlessly chase my dreams and for following me wherever they may lead.

Acknowledgments reflect the views of the author and are not endorsed by committee members or Oklahoma State University.

Name: ZACKERY JAMES BYCKO

Date of Degree: MAY, 2023

Title of Study: EFFECT OF ADDITIVE-MANUFACTURED FUEL GRAIN GEOMETRY ON SMALL-SCALE HYBRID ROCKET PERFORMANCE

Major Field: MECHANICAL AND AEROSPACE ENGINEERING

Abstract: This paper presents a parametric study of additive-manufactured fuel grain geometry on small-scale hybrid rocket performance. The motivation of this study is to understand and increase hybrid rocket performance to be a more viable option when compared to solid and liquid rocket propulsion systems. Hybrid rocket engine systems consist of two different propellant components: a solid fuel and a liquid or gaseous oxidizer. This research evaluates the use of additive-manufactured polylactic acid filament as a potential propellant in a hybrid rocket propulsion system. Additive-manufactured fuel grains provide an engine system capable of reduced operational expenses, reduced operational hazards by having separate fuel and oxidizer, and highly tailorable rocket performance with custom grain geometry and composition. On top of all that, these fuel grains provide a safer alternative to the volatile nature of solid rocket propellants, as well as simplifying manufacturing and easing storage requirements associated with fuel grains. The goal of this study is to observe the variances in hybrid rocket engine performance as a function of differing infill densities and infill geometries present within the fuel grain. Because the practice of additive-manufactured fuel is new, the parameters associated with manufacturing fuel grains are largely not well understood when related to rocket engine performance. By adjusting the infill percentage and infill shape print pattern of the fuel, different thrusts, burn times, and burn rates can be achieved due to the change in surface area, density, and its reaction with the oxidizer flow. Performance variances were evaluated on a 38-mm diameter hybrid rocket engine system over fuel grains with three different infill densities of 30%, 50%, and 70% with cubic infill geometry. Performance variances were then evaluated on the same engine system over fuel grains with three different infill geometries of cubic, triangular, and concentric with a 50% infill density. Small sample ANOVA testing at a 95% confidence interval concludes that there are significant statistical differences in the mean for average thrust, total impulse, specific impulse, and regression rate for the infill density testing campaign. However, small sample ANOVA tests were unable to deduce a significant statistical difference in the means for any of the infill geometry cases. Although no statistical significance was present, certain trends were still able to be deduced which warrants testing for larger scale HREs. Follow-up work includes increasing the scale of the HRE in diameter and case length, comparisons between PLA and ABS in terms of performance and consistency, and variation of port geometry and its effects on thrust profiles and regression rate.

TABLE OF CONTENTS

Chapter Page

LIST OF TABLES

Table Page

LIST OF FIGURES

Figure Page

CHAPTER I

INTRODUCTION

1.1 Introduction and Motivation

Historically, hybrid rocket engines (HREs) have been overlooked due to poor performance or efficiency. An HRE system is a classification that combines the characteristics of both solid and liquid propulsion systems. In an HRE, one of the components, either fuel or oxidizer, is in a solid state while the other is in a gaseous or liquid state. This combination of states allows the system to utilize benefits from both solid and liquid rocket engines, creating a unique envelope that neither system could operate in alone. Compared to solid rocket motors, HREs provide on-demand start and stop capabilities, and reduced storage hazards by storing the oxidizer and fuel separately. Hybrid engines differ from liquid engines by offering a less hazardous system with greater fuel density. Due to having only one liquid or gaseous compound, HREs offer a cheaper and simpler option where throttling is necessary. Figure 1 displays a simplified visual representation of each rocket propulsion system. HRE systems have a variety of applications, including sounding rockets, suborbital and orbital launch vehicles, and rocket assisted takeoff (RATO). These applications appeal to both military and commercial providers, making hybrid rocketry an interesting research topic over the last few decades.

SpaceShipOne (SS1) was an experimental space vehicle designed and developed by Scaled Composites, an aerospace company founded by aircraft designer Burt Rutan in 1982 [2]. SS1 was part of a broader vehicle program known as Tier One, made up of SS1, a launch aircraft coined WhiteKnight, an HRE system, and an avionics suite. SS1 was entered into the Ansari

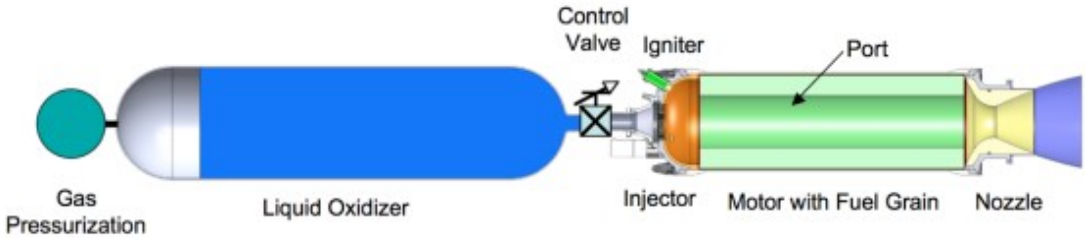

Figure 1: Standard HRE Configurations. [1]

X Prize, a space competition in which the X Prize Foundation offered $ 10 million for the first private organization to launch a reusable manned aircraft into space twice within the span of two weeks. Thousands watched as SS1 reached an apogee of over 350-thousand feet in the fall of 2004. This date represents one of the first successful employments of an HRE. This configuration was so successful that Sir Richard Branson of Virgin Galactic partnered with Burt Rutan to build SpaceShipTwo and WhiteKnightTwo. More recently, companies like Firehawk Aerospace have begun work on HREs for potential military applications.

Figure 2: SS1 and its designer, Burt Rutan. [2]

Additive-manufacturing has brought a resurgence of research into rocket propulsion sys-

tems due to the versatility this manufacturing process can provide. Additive-manufacturing, more colloquially known as 3-D printing, is the process of layering material onto a flat surface, called a build plate, through a series of complex computer-controlled algorithms. Additive-manufacturing allows for a safe, scalable, dependable, and automated process that produces parts with tighter tolerances and less waste. Hybrid and liquid systems usually require small intricately designed components that would be too difficult to design by hand, such as nozzles with internal cooling passages and swirl-inducing injectors, that can only be additive-manufactured.

More recently, the use of additive-manufacturing has become an attractive candidate to design and fabricate fuel grains for HREs. A fuel grain is a cylindrical segment of solid fuel that varies in length and diameter based on the amount of thrust the propulsion system produces. Advances in additive-manufacturing technologies have allowed for the ability to design and rapidly produce HRE fuel grains with countless parameters to fine-tune the performance and operability of the engine. Due to this technology, the door to a wide research field as opened. Materials such as ABS, paraffin, and others have shown potential as high-energy plastics that, when combined with oxidizer, show potential to succeed has a hybrid rocket fuel. Polylactic acid (PLA) is a cheap, high-density thermoplastic that can be economically produced from renewable resources. Utilizing additive-manufacturing in HRE fuel provides other inherent characteristics that can alter the way in which the fuel grain burns. Control of those computer algorithms modifies the amount, known as infill density, and pattern, known as infill geometry, of material added to the component. Changes in infill density and infill geometry alter burn characteristics of the fuel grain. Representations of these traits can be seen in Figure 2. By way of additive-manufacturing, fuel grains with complex core geometries can be made to create HREs with unique burn characteristics to accommodate a wide range of mission profiles.

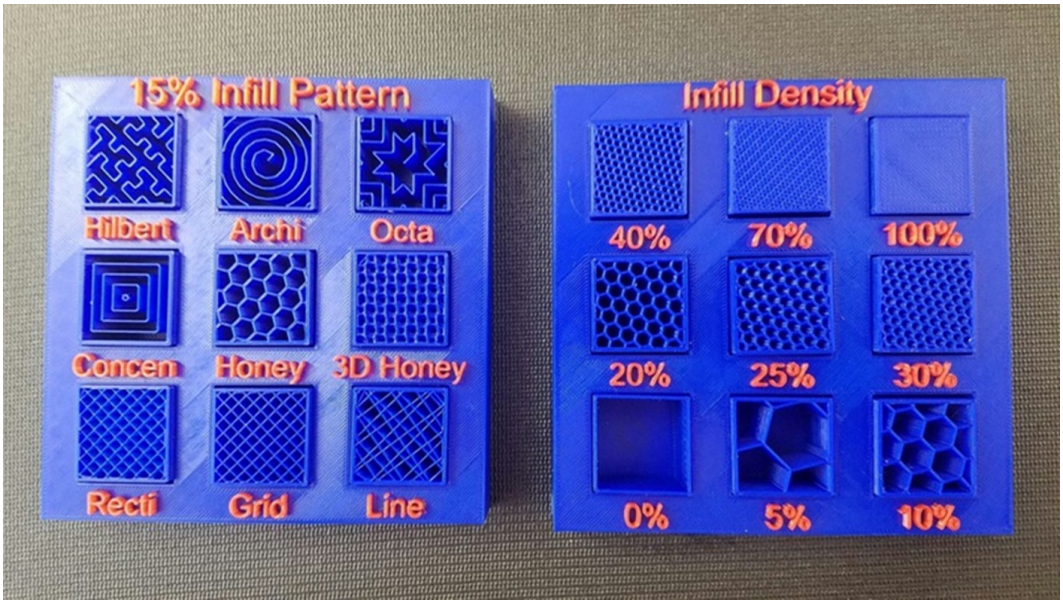

Figure 3: Infill Patterns and Density. [3]

1.2 Research Objectives

The scale explored in this work consists of a rocket engine with a 38-mm diameter casing. This size represents the lower end of what is considered high powered rocketry, with thrust measurements ranging from ten to twenty-five pounds of thrust. Figure 3 depicts casings of various sizes to serve as a reference for the scale.

Due to this technological advancement being rather new, the design space for additive-manufactured fuel grains is vast. Printers are being updated with software that allow them to print in new patterns and with different materials. Thus, there is a critical need to characterize the effects of these geometries on the performance and operability of HREs.

The research objectives are as follows:

1. Evaluate the effects on thrust, impulse, and regression rate by varying infill percentage from 30%, 50%, and 70% with cubic infill geometry utilizing an additive-manufactured PLA fuel grain with NOS as oxidizer in a 38-mm HRE system.

2. Evaluate the effects on thrust, impulse, and regression rate by varying infill geometry at cubic, triangular, and concentric with 50% infill density utilizing an additive-

Figure 4: 76-mm (left), 54-mm (center), and 38-mm (right) Diameter Rocket Casings.

manufactured PLA fuel grain with NOS as oxidizer in a 38-mm HRE system.

CHAPTER II

BACKGROUND AND THEORY

2.1 Hybrid Rocket Engine Fundamentals

The performance of all rocket engines can be evaluated based on a set of several key performance parameters. Typical measurables for rocket engines include mass flow rate ($\dot{m}$), thrust (F), burn time (t_b), total impulse (I), and specific impulse (I_{sp}). Due to the nature of hybrid rockets, there are other performance parameters that apply known as oxidizer mass flow rate ($\dot{m}_{ox}$), and feed pressure (P_o). The combination of these different parameters is related to determining what type of rocket is used and what configuration that rocket is used in, especially regarding propellant composition and nozzle geometry. Thrust is a measure of the reaction force produced by combustion of the fuel and oxidizer within the engine, which expels hot gases out of the nozzle. Specific and total impulse are measures of the energy that the propellant releases over the length of the burn. Burn time specifies the length of the burn for a rocket engine, while burn rate refers to the rate at which the propellant burns to completion within the engine. To accurately understand these forces at play, the control volume in question must be considered. For this analysis, a hybrid rocket engine with all necessary plumbing is mounted on linear bearings with the forward closure direct transferring the force into the load cell. If we consider only the engine and load cell, we can include the propellant temperature, pressure, and other properties that occur within the chamber. Figure 5 depicts these relationships below with the consideration of pressure forces at the nozzle exit.

Mass flow rate ($\dot{m}$), often times also referred to as mass flux, is a measure of the rate a fluid

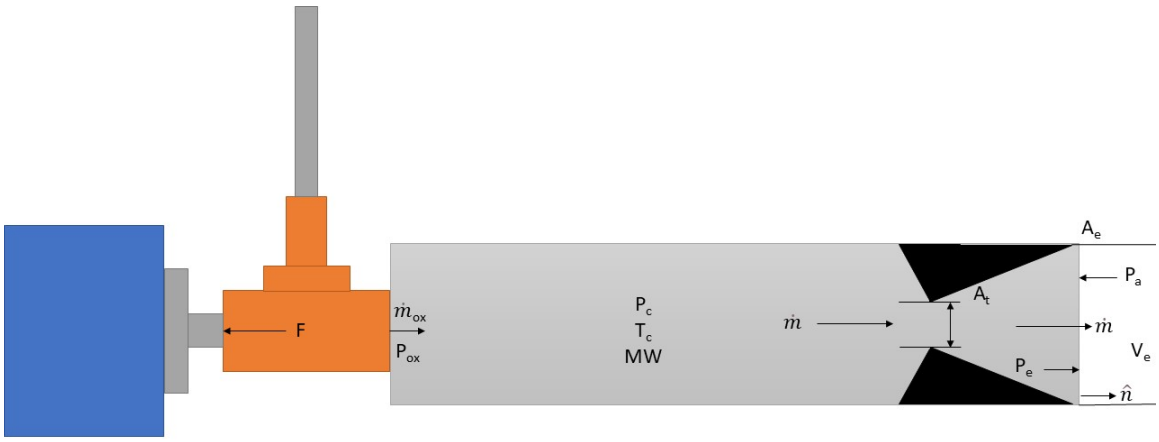

Figure 5: Hybrid Rocket Engine Control Volume.

flows through a certain cross section during a length of time. Mass flow rate is an important metric for engines as it determines the amount of substances used during the combustion process that are used to determine thrust, efficiency, and other performance metrics. In hybrid rocket engines, mass flow rate is commonly applied to the fuel and oxidizer. Knowing the values of these parameters is pivotal in determining fuel regression rates and oxidizer remaining in supply. Mass flow rate is defined by Equation 2.1.1, where (ρ), (A), and (v) are equal to the density of the fluid, the area of the cross section, and the velocity of the fluid in that cross section, respectively. This equation is applied to many different orifices, which results in many different combinations of areas, velocities, and densities that work together throughout the system.

$$\dot{m} = \rho * v * A \tag{2.1.1}$$

By using Newton's second law of motion, while also assuming the flow field is steady and one-dimensional, the momentum equation can be rearranged and simplified to be equated to the sum of pressure and momentum forces exiting the control volume. This simplification

is characterized in a new form shown in Equation 2.1.2.

$$F = \frac{\dot{m} * V_e}{g_c} + (P_e - P_a) * A_e \tag{2.1.2}$$

The right side of the simplified thrust equation can be separated into two separate pieces, each with their own unique contribution to overall thrust. Mass flow rate multiplied by the normal component of exit velocity divided by the gravitational constant is known as momentum thrust, while the difference in pressures multiplied by the exit area is known as pressure thrust. The momentum term will account for the majority of the thrust. The second term is a tuning mechanism to determine the total thrust with respect to altitude, and can be positive, negative, or zero depending on the design of the exit pressure of the nozzle. Ideal nozzle performance occurs when the ambient pressure matches the exit pressure, and the exit velocity of the nozzle is maximized. This results in the pressure thrust being equal to zero. Most nozzles are over-expanded at sea level due to the high ambient atmospheric pressure. This phenomenon is due to the atmospheric pressure being greater than the nozzle exit pressure, causing push back on the exhaust plume, producing a negative pressure thrust. A positive pressure thrust does not always mean better performance, however. Anything other than perfectly-expanded nozzles do not perform with an ideal normal velocity component. Refer to Figure 6 for visual representations of different modes of nozzle performance.

An engine's burn time (t_b) can be characterized by using the thrust profile during the duration of its burn. A normal thrust profile for a rocket engine is characterized by three distinct stages of an engine's burn: rise, sustain, and fall. During the rise time, the igniter will ignite the engine causing a sharp increase in pressure and thrust. Depending on the propellant composition and geometry of the grain, the engine can exhibit distinctive characteristics during the sustainment period of the burn. Motors can exhibit progressive, regressive, or neutral burn profiles depending on the slope of the thrust curve in the sustainment period. The end of the burn time is characterized by a sharp drop in thrust, indicating the end of the burn period. A more in-depth look at engine burn time can be seen in Figure 7 for

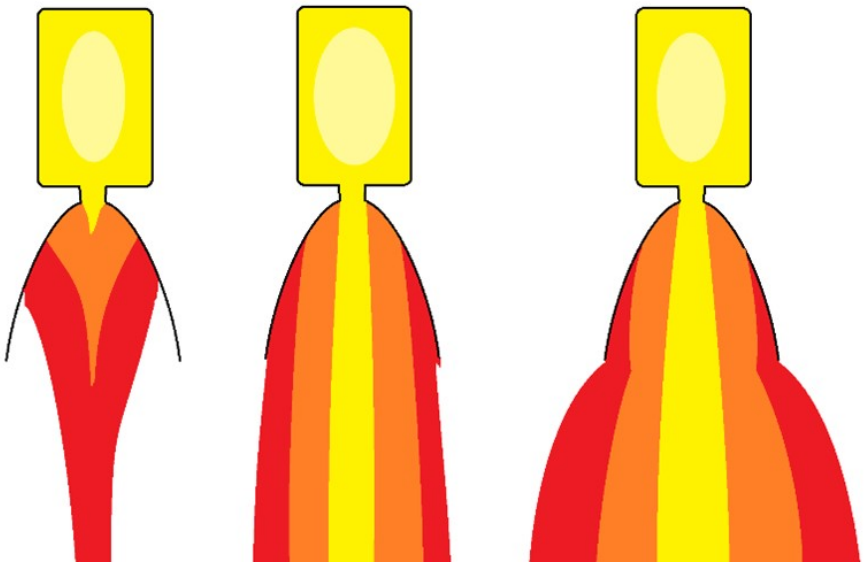

Figure 6: Over-expanded (left), Perfectly-expanded (center), and Under-expanded (right) Nozzles.

reference. Units associated with an engine's burn time is seconds, or (s).

Total impulse (I) is characterized as the integral of thrust with respect to the burn time. Total impulse is a metric used to determine the overall energy a rocket propulsion system has to offer and is commonly employed in determining the energy required for various stages during a rocket's mission. The units for total impulse are a force multiplied by time, such as $(N * s)$ or $(lbf * s)$. Equation 2.1.3 serves as a reference to the relationship of thrust, burn time, and total impulse. This value can also be calculated by multiplying the average thrust by the engine's burn time.

$$I = \int_0^{t_b} F\,dt = \bar{F} * t_b \tag{2.1.3}$$

Specific impulse (I_{sp}) is the ratio of a rocket's total thrust per unit weight flow of propellant through its nozzle. This metric serves as a propulsive efficiency, where the higher the specific impulse, the more efficient the engine system is at producing thrust per propellant weight. Due to having a solid fuel and liquid or gaseous oxidizer, hybrid rocket engines typically have a middle of the road specific impulse. This is because the solid fuel portion

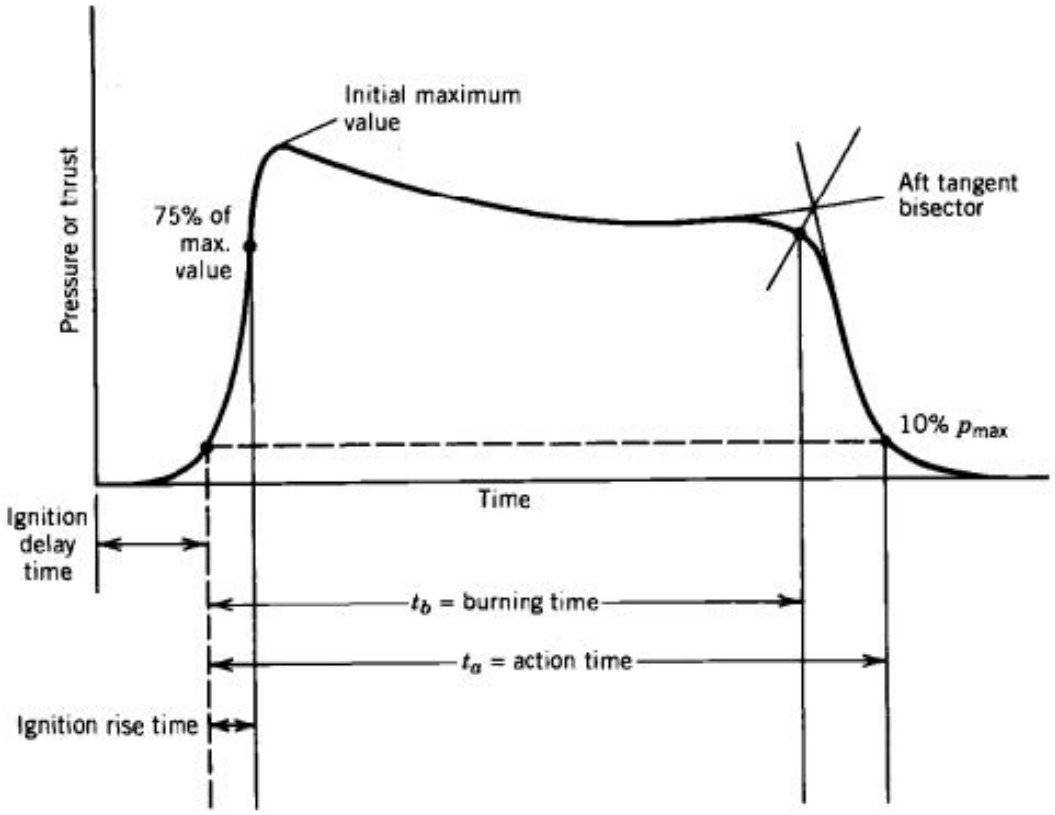

Figure 7: An Expanded Look at Burn Time. [4]

is usually heavy compared to other liquid fuels. The expression for specific impulse can be shown in Equation 2.1.4 for reference. The units for specific impulse are expressed as seconds, or (s).

$$I_{sp} = \frac{F}{\dot{w}} \tag{2.1.4}$$

Due to the nature of hybrid rocket engines, the burn rate of the fuel must be measured differently than both solid and liquid systems. Regression rate $(\dot{r})$ is the measure of the length the solid fuel grain regresses, or burns away, over time. Typically, hybrid rockets are characterized as having low regression rates which is not good for rocket performance. Regression rate is an important metric for hybrid rocket engines to compute fuel flow and overall performance. For this study, regression rate is represented by its longitudinal component and calculated using the mass flow rate of fuel and oxidizer. The time-averaged

longitudinal regression rate is shown in Equation 2.1.5. Note that these values are all in terms of the fuel.

$$\dot{\bar{r}} = \frac{\dot{m}_{fuel}}{\rho_{fuel} * 2 * \pi * \bar{r}_{port} * L} \tag{2.1.5}$$

($\bar{r}_{port}$) is known as the mean fuel combustion chamber radius. This value can be calculated using the initial port radius of the fuel ($\bar{r}_0$), the total mass loss of the fuel (ΔM), and length of the combustion chamber (L). Equation 2.1.6 can be seen showing the relationship between these values.

$$\bar{r}_{port} = \sqrt{r_0^2 + \frac{\Delta M}{\rho_{fuel} * \pi * L}} \tag{2.1.6}$$

2.2 Hybrid Rocket Engine Combustion

Due to hybrid rocket engines having a combination of solid fuel and liquid or gaseous oxidizer, the combustion they experience is unlike its solid or liquid counterparts. Figure 8 provides a close-up view of the different modes of the boundary layer that are present in hybrid rocket engine combustion. Boundary layer combustion is the primary mechanism of hot gas generation in HREs. Upon ignition, a diffusion flame forms over the fuel surface along the length of the port. The combustion is sustained by heat transfer from the flame to the solid fuel causing continuous fuel vaporization until the oxidizer flow is turned off [1]. On top of a velocity gradient that is present within the flow, there is a temperature gradient based on the mixing that occurs between the fuel and oxidizer during the combustion process. Below the flame zone, there is a fuel-rich portion of flow while above the flame zone, there is an oxidizer-rich zone. The flame zone is characterized by the highest combustion temperature in the flow, which occurs where the oxidizer to fuel ratio (O/F) is the most ideal for the given fuel and oxidizer combination. The flame height is set by the competition between the energy from the flame vaporizing the fuel, the turbulent boundary layer development along the fuel port, and the blowing of the fuel of the gases departing the surface [5].

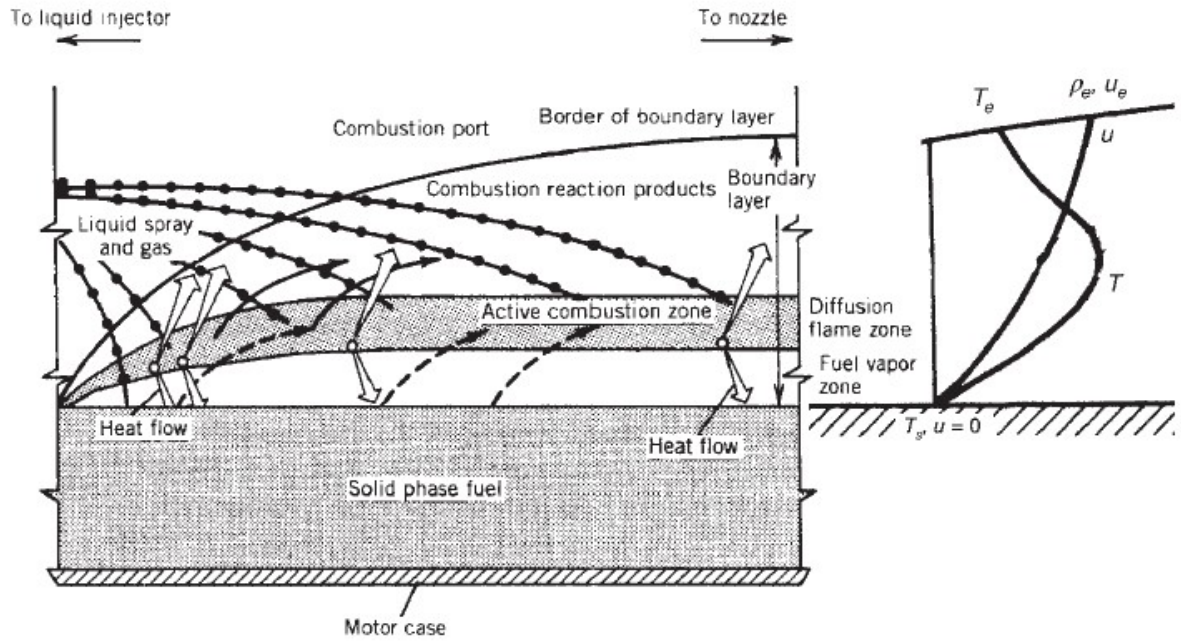

Figure 8: Hybrid Rocket Engine Fuel/Oxidizer Boundary Layer. [6]

2.2.1 Regression Rate Behavior

Fuel regression rate behaviors are linked to mass flux (G), where different regions can be identified within different mass flow regimes. The middle region is where regression rate is diffusion dominated. When (G) gets too high, the combustion process is controlled by the chemical kinetics and not diffusion. This is where the regression rate becomes pressure dependent and eventually reaches an upper bound, known as the flooding limit. The flooding limit is characterized by very oxidizer-rich conditions and will extinguish the flame. At too low of a (G) value, convective heat transfer no longer plays a significant role and will be dominated by radiation [7]. Figure 9 outlines the mass flux regime phenomenon with respect to regression rate.

Marxman laid the foundation for describing and understanding fuel regression rate. According to his studies from 1963-1965 [8, 9, 10], regression rate is most accurately correlated to the convective heat transfer from the boundary layer to the surface of the fuel grain. In most cases, regression rate is assumed to be constant across the length of the grain. There-

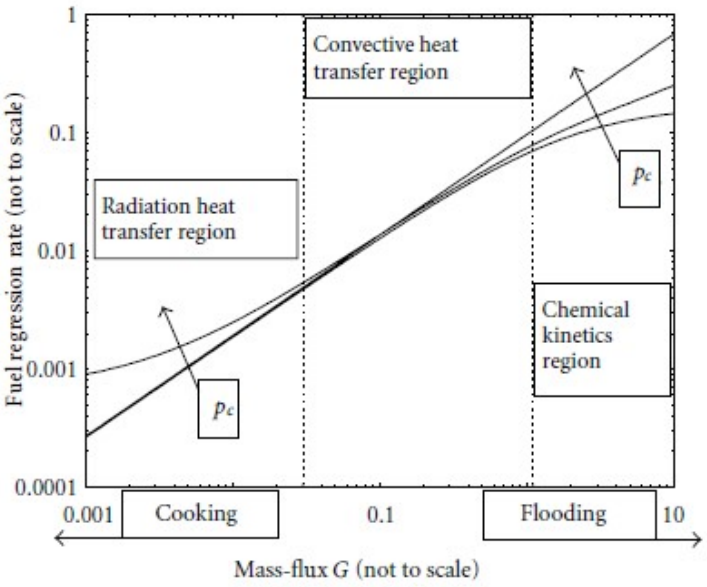

Figure 9: Typical Regression Behavior Based on Mass Flux. [7]

fore, it is a safe assumption to correlate regression rate with mass flow entering the solid fuel port. Equation 2.2.1 outlines the correlation Marxman and company derived, where $(G_O = \frac{\dot{m}_O}{A_p})$, $(\dot{m}_O)$ is mass flow of oxidizer, and (A_p) is area of the fuel grain port.

$$r = a * G_O^n \tag{2.2.1}$$

(a) and (n) are both experimentally-derived constants for a given (G_O) range and depend on engine dimensions, fuel grain geometry, injector geometry, and internal flow features of the HRE [7].

2.3 Hybrid Rocket Engine Advantages and Disadvantages

Hybrid rocket engines experience a wide variety of advantages and disadvantages when compared to their solid and liquid counterparts that apply to distinct aspects of the engine's design, performance, and operability. Some of the earliest work with rockets involved HREs due to the simplicity, safety, cost, and versatile operation envelope.

2.3.1 Advantages

One of the earliest studies on HREs was performed by General Electric in 1956, which outlined an HRE employing a 90% hydrogen peroxide oxidizer and polyethylene fuel "solid-liquid" rocket [11]. The reasoning that led to this employment method and its advantages were also outlined. Compared to solid rocket motors, HREs exhibit theoretical higher specific impulse and the ability to throttle the engine for better control during burn. The ignition range is smooth over a wide range of oxidizer to fuel ratios. When compared to their liquid counterparts, HREs require much less mechanical sophistication, due to only having one liquid or gaseous propellant. Due storing the fuel and oxidizer separately, HREs are typically safer than both liquid engines and solid motors. Separate storage also allows for ease of storage requirements usually associated with solid fuels. Hybrid rockets also do not typically have toxic exhaust products, which makes them better for the environment than solid motors and liquid engines. The combination of these traits allows for a cheap option where throttling is necessary. Table 1 shows a more in-depth breakdown of HREs advantages compared to solid and liquid rocket systems.

Table 1: Advantages of Hybrid Rocket Engines over Solid and Liquid.

Category	Solid	Liquid
Simplicity	Chemically simpler	Mechanically simpler
Safety	Reduced explosion hazards	Reduced fire/plumbing hazards
Operability	Restart/throttling capabilty	Only one liquid
Performance	Greater theoretical (I_{sp})	Greater fuel density
Environmental	Less toxic exhaust products	Less contamination hazard
Cost	Reduced development/storage cost	Reduced operational cost

2.3.2 Disadvantages

Although there are quite a few advantages that make hybrid rockets seem attractive, they are usually not implemented due to the drawbacks that come with the system. One of the main hindrances of HREs is that the combustion process relies on a slow mechanism of fuel melting, evaporation, and diffusive mixing shown in Figure 8. As a rough comparison, solid rockets at a typical combustion pressure may be near $1.0cm/s$ whereas HREs using a classic polymeric fuel may have a regression rate on the order of $0.1cm/s$ [1]. Solid rocket motors also lack plumbing and turbomachinery because they have no moving fluids. This makes them the option of choice when thrust-to-weight ratio is of consideration. Due to still having one solid fuel grain, liquid systems can exhibit a higher specific impulse than HREs, making liquid systems the standard for lightweight rocket engines. Due to not having the best thrust to weight ratio, nor being able to produce the most efficient thrust, HREs are rarely chosen in the systems of today.

As with most chemical combustion processes, an ideal mixture ratio exists. Due to the boundary layer effects on temperature and velocity, a non-uniform burning profile occurs along the length of the fuel grain. As the flow within the fuel grain port fully develops, it experiences more consistent burning with better mixing as the flow proceeds through the casing towards the nozzle. Better mixing of fuel and oxidizer leads to a higher combustion temperature. As the combustion temperature rises, so does the vaporization rate of the solid fuel, which causes the fuel grain to burn faster towards the nozzle than the injector. This phenomenon is known as O/F shift. O/F shift makes it difficult to design for a perfect fuel grain and is an inherent disadvantage of a hybrid rocket propulsion system that results in non-optimal performance.

2.3.3 Solutions

There are known paths to solutions to low regression rates. One of these are the use of fuels that experience good vaporization during the process of combustion. In the 1990s, the U.S.

Air Force studied cryogenic fuels designed for HREs. In their efforts, they discovered pentane burns around 3 to 4 times faster than normal fuels. Pentane produces a thin, low viscosity, low surface tension liquid layer on the fuel surface during combustion. This instability driven by the shearing effect of the oxidizer flow in the port leads to the entrapment of fuel droplets into the gas stream, increasing overall fuel mass transfer rate. This mechanism acts as continuous spray injection distributed along the port, which leads to much higher regression rates than conventional polymeric fuels that rely solely on evaporation [1]. Lower required energy for vaporization results in a more uniform burn profile throughout the fuel grain. This mechanism is depicted in Figure 10.

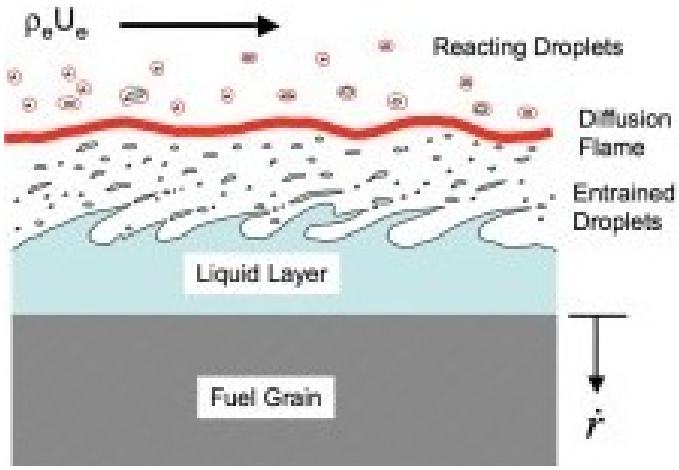

Figure 10: Liquid Layer Mechanisms. [1]

Another way to compensate for low regression rates is through surface area manipulation of the fuel grains. The more surface area in contact with the oxidizer, the faster the solid fuel grain will burn. This can be accomplished by multi-port grains depicted in Figure 11 [1]. One of the main problems with this is that the volume of the fuel decreases, which decreases the amount of energy the fuel can store. Most attempts to improve fuel regression rate involve increasing heat transfer to the fuel surface. This can be done by inducing turbulence to the fuel by adding roughness. Complex helical geometries have shown to increase regression rates due to producing a more turbulent flow that results in better mixing of the fuel and oxidizer [12].

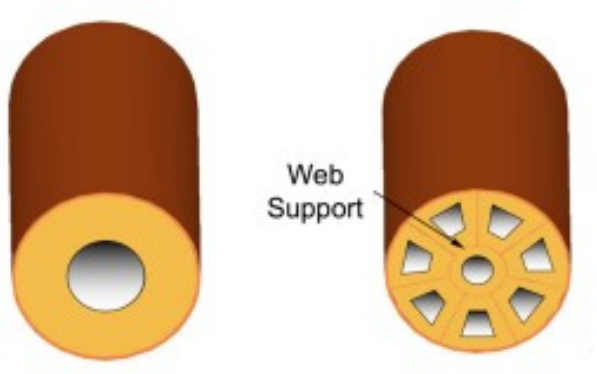

Figure 11: Single Versus Multi-Port Fuel Grains. [1]

2.4 Hybrid Rocket Engine Types

While hybrid rocket engines exhibit properties from both solid and liquid engines, there are many different configurations to employ these characteristics. Ttypes of hybrid engines include monopropellant, bi-propellant, and even reverse hybrid engines. A reverse hybrid is a hybrid that employs a solid oxidizer with a liquid or gaseous fuel, which was first attempted by William Avery in 1952 [13]. The most common employment of the hybrid engine is a solid fuel and liquid or gaseous oxidizer, due to its simplicity, reliability, and cost-effectiveness. These reasons are why this configuration was chosen for this study.

2.5 Additive-Manufacturing Overview

Additive-manufacturing (AM) is the process of building an object by adding material until it is the desired shape. Technically, this encompasses any build process that involves adding material, such as molding, but more recently has been used as the production name to three-dimensional (3-D) printing. 3-D printing is a computer-controlled process that creates highly-customizable 3-D objects by depositing layers of material. While concepts date back to the early 20^{th} century, AM technology has not provided reliable and functioning parts until recently. AM parts usually begin in a computer-aided design (CAD) software. Common CADs include SolidWorks, CATIA, and SketchUp. These CAD softwares use pre-

cise geometry and a series of sketches, extrusions, and cuts, along with many other possible design processes, that ultimately assist the user in designing a part with precise geometry. Once the part is designed, it is saved and sent through a slicer software that translates the CAD design into a layer-by-layer design that interfaces with the 3-D printer. This design is then sent to the 3-D printer, where it executes the design by layering material in certain patterns to achieve the desired part geometry. There are a wide range of 3-D printer types and materials, each providing its own set of benefits and drawbacks.

2.5.1 Common AM Techniques

Vat Photopolymerization

Vat Photopolymerization, or stereolithography apparatus (SLA), is when a vat of liquid photopolymer resin is cured through the selective exposure to light (via laser or projector) which initiates polymerization and converts exposed areas into solid parts [14]. SLA prints typically use UV-curable photopolymer resins, feature high levels of accuracy and complexity, accommodates large build areas, and allows for a smooth surface finish. This was the first commercialized AM printing technique. An example of SLA printing can be seen in Figure 12.

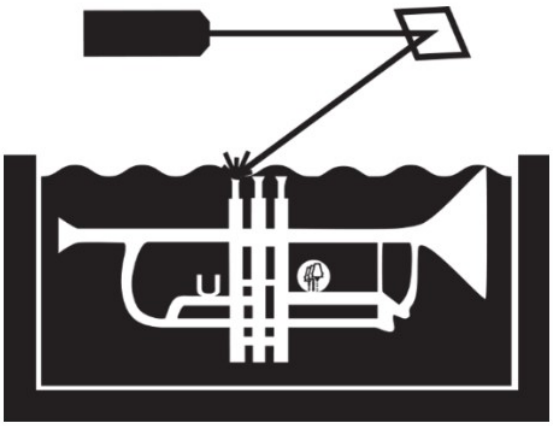

Figure 12: SLA Printing Technique. [14]

Powder Bed Fusion

Powder Bed Fusion is one of the most employed AM techniques. Also known as selective laser melting (SLM), powdered material is consolidated by melting it together using a heat source such as an electron beam. The powder surrounding the consolidated part acts as support material for the overhanging features [14]. SLM prints have a wide range of materials such as plastics, metals, ceramics, and even sands. This AM technique allows for a high complexity in part shape. An example of SLM printing can be seen in Figure 13.

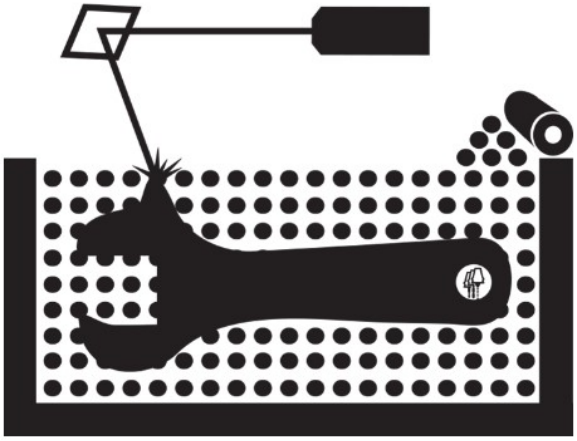

Figure 13: SLM Printing Technique. [14]

Directed Energy Deposition

Directed Energy Deposition (DED) is an AM technique that is most closely related to welding. DED printers utilize powder or wire that is fed into a melt pool which has been generated on the surface of the part where it adheres to the underlying part or layers by using an energy source such as an arc, laser, or electron beam [14]. DED printing benefits include no axis limitation, allows for repairs, and the ability to use multiple materials in a single part. An example of DED printing can be seen in Figure 14.

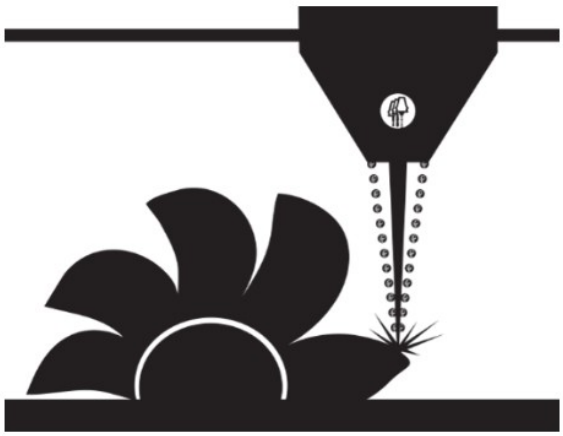

Figure 14: DED Printing Technique. [14]

Material Extrusion

Of the many printing techniques, material extrusion is the most widely used AM printing technology due to its ease of use. Material is extruded through a nozzle or orifice in tracks or beads, which are combined into multi-layer models. Varieties include heated thermoplastic extrusion and syringe dispensing [14]. Commonly known as Fused Deposition Modeling (FDM), the benefits for this AM technique are wide. It is conceptually simple, does not require health concerning glue or solvents [15], and most of the printing apparatus is cheap and tabletop size [16]. Typical materials for this technique are thermoplastic filaments and liquids. That allows for parts that are very economical, can be printed in multiple colors, offer strong structural properties, and can usually be used in office environments. The basic functioning of FDM can be seen in Figure 15. A thermoplastic filament is continuously fed into a small heated chamber where it melts, becoming a highly viscous fluid. The melt is then extruded through a nozzle and then deposited layer-wise on a heated table, following the pattern specified by the CAD file and slicer software [17].

The process by which FDM printing occurs depends on a list of parameters that define the way the part is printed. These parameters can be seen in Table 2 with a brief description. Because FDM printers have so many different parameters by which the designed parts are constructed, the design space is large. Nozzle and filament diameter are usually correlated to

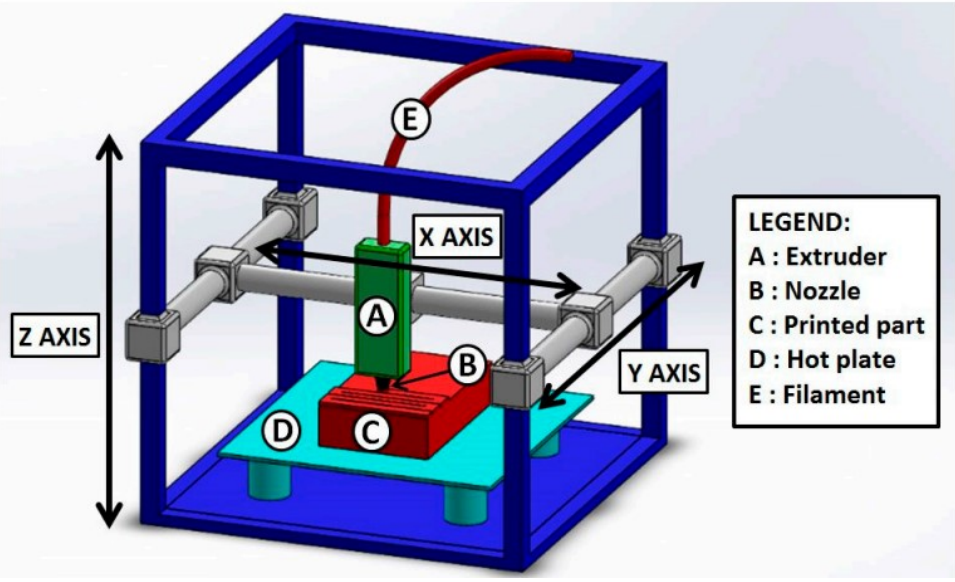

Figure 15: Schematic of Typical FDM Setup. [17]

the type of filament or size of print. Infill parameters such as geometry and density specify the way in which the prints are constructed and with how much filament. These parameters affect structural properties as well as weight. FDM printers were chosen due to the largely undiscovered design space, along with its cost-effectiveness, ease of use, and minimal health risk.

2.6 Hybrid Rocket Engine Composition

The composition of fuel and oxidizer in a hybrid rocket engine system plays a role in the overall performance and operability of the system. As seen in an earlier section, there is a delicate balance of energies at play in hybrid rocket combustion that produces the best burn characteristics. Choosing the best combination for performance may be a long and tedious process. However, there are different perspectives to consider when deciding the best composition for the application, such as cost, storability, and simplicity. Depending on the type of hybrid engine, the fuel and oxidizer may come in many different combinations, and sometimes even different states within the same component. There are other materials, aside from the main fuel material, which can be added into hybrid fuel to change the density

Table 2: FDM Printing Parameters. [17]

Parameter	Description
Nozzle Diameter	Size of exit orifice of nozzle
Filament Diameter	Size of the filament required by nozzle
Nozzle Temperature	Temperature required by the nozzle
Build Plate Temperature	Temperature required by the build plate
Layer Thickness	Thickness of the layers deposited by nozzle
Infill Geometry	Internal structure of the printed component
Infill Density	Material percentage filling the component
Number of Layers	Number of wall layers deposed by the nozzle

or alter burn rate characteristics.

2.6.1 Fuel

The fuel in an HRE is usually responsible for providing the energy needed for thrust during combustion. Stereotypical fuel for hybrid rocket engines is generally comprised of solid hydrocarbon materials due to them having the molecules necessary to create high flame temperatures. The most widely used hybrid rocket fuel is Hydroxyl-Terminated Polybutadiene (HTPB). One of the main problems with HTPB is the intensive manufacturing process that takes place with the fuel grain. HTPB must be uniformly mixed in a liquid form with other additives, degassed in a vacuum, cast into its desired shape, then left to cure for an extended period before it is ready for use. This manufacturing process often leaves small amounts of gas trapped in the fuel grain, causing density impurities that could affect performance. Because of the nature of the casting process, it is difficult to cast complex internal geometries.

Due to the recent advances in additive-manufacturing, hybrid rocket engines are being explored with other materials to gain further knowledge on the relationships at play between fuel and oxidizer. FDM printers have allowed for complex internal geometries,

automated manufacturing, and more consistent results in grain density. The use of additive-manufacturing has allowed for the design space of solid fuel grains to be limitless, allowing very customizable fuel grains for a wide range of mission profiles. Various parameters, such as infill percentage and infill geometry, can be applied to fuel grains that allow for different regression rates and thrust values that cater to the mission. This process is additive and leaves very little waste because of that.

FDM printers have a wide variety of filaments available, each with their own properties that are used for different applications. The most common types of filament employed today are PLA, Acrylonitrile Butadiene Styrene (ABS), Polyethylene Terephthalate Glycol (PETG), nylon, and others. The structural, thermal, and mechanical properties of these materials can be seen in Table 3.

Table 3: Structural, Thermal, and Mechanical Properties of Common FDM Materials. [18]

Material	Crystallinity	Density (g/m^3)	Yield Strength (MPa)	Print Temp ($^\circ C$)
ABS	Non-crystalline	1010	55	220 - 260
ASA	Non-crystalline	1000	40	220 - 250
PETG	Moderate	1230	50	230 - 250
PLA	Moderate	1225	63	190 - 220
Nylon	Moderate	1150	55	220 - 260
PP	High	980	40	230 - 260

ABS is an inexpensive filament material that already has proven applicability as a hybrid rocket fuel. ABS has been shown to be more consistent than HTBP in hybrid rocket combustion due to the more accurate manufacturing process and high energy content of butadiene [19]. Another intriguing FDM filament for hybrid rocket applications is PLA. PLA is similar to ABS in its mechanical properties but has a large advantage in its environmental impact. PLA is a thermoplastic polyester with a chemical formula of ($C_3H_4O_2$) and is the most common FDM filament for its good mechanical properties and biodegradability.

PLA is principally produced from starch saccharification, lactic acid fermentation, oligomerization, cyclic monomer, and ring-opening polymerization of the cyclic monomer. PLA is easily processed on standard plastics equipment and can be made annually from renewable resources to yield articles for use in either the industrial packaging field or the biocompatible/bioabsorbable medical device market [20]. PLA is degraded by simple hydrolysis of the ester bond and does not require the presence of enzymes to catalyze this hydrolysis. The rate of this degradation is dependent on the size and shape of the article, the isomer ratio, and the temperature of the hydrolysis [21]. Table 4 compares the material properties of PLA, ABS, and HDPE, a traditional hybrid rocket fuel.

Table 4: Material Properties of ABS, PLA, and HDPE. [22]

Material	Repeating Unit	Ignition Temperature ($°C$)	Density (g/m^3)
ABS	$(C_3H_3N, C_4H_6, C_8H_8)_n$	466	1030
PLA	$(C_3H_4O_2)_n$	388	1240
HDPE	$(C_2H_4)_n$	340	970

Note a slight variation in densities occur between Tables 3 and 4. This could be due to environmental differences or differences in the way these materials were evaluated. The ignition temperature of ABS is $466°C$ [23], which is much higher than the other materials listed on this table. A high ignition temperature is not desirable, as it takes more energy to complete the combustion process. High combustion temperatures and pressures could be problematic as they are more difficult to achieve. Further studies have shown that ABS produces several volatile organic compounds in much higher concentrations at a temperature around $250°C$ [24, 25], which is much lower than its ignition temperature. PLA presents a lower ignition temperature at $388°C$ and higher density than ABS. A higher density with a lower ignition temperature is desirable because it does not take as much energy to burn, and higher density material creates more thrust due to higher available mass flow of the fuel. PLA has been known to emit harmful combustion products, but at lower levels than other plastic

materials and leaves no residue [26]. Leaving no residue is an attractive characteristic of PLA, as it does not present a harmful impact on reusable hybrid rocket casings. Another study on the thermal degradation and combustion properties of common biodegradable polymers shows that PLA has a combustion temperature of $382°C$ in a nitrogen environment and $385°C$ in an oxygen environment [27]. This study is useful because nitrogen and oxygen are the two elements that make up Nitrous Oxide (N_2O), a common oxidizing agent for hybrid rocket propulsion.

2.6.2 Oxidizer

Oxidizer is used to control the intensity and rate of the combustion process. There are distinct characteristics to consider when deciding on an oxidizer for a hybrid rocket system. Because none of these oxidizers encompass all desirable properties, the selection of an oxidizer is usually a compromise between several factors such as availability, cost, storage requirements, hazards, and performance [6]. The most common oxidizers for hybrid rocket engines are Liquid Oxygen (LOX), Ozone, Nitrous Oxide (NOS), Dinitrogen Tetraoxide (NTO), Nitric Acid (IRFNA), and Hydrogen Peroxide. Thermochemical properties of these well-known oxidizers reacted with HTPB can be seen in Table 5.

Table 5: Thermochemical Properties of Common Oxidizers Reacted with HTPB. [6]

Oxizider	Chemical Formula	Type	Boiling Point $°C$	Density $\frac{g}{cm^3}$	$\Delta_f H^a(\frac{kcal}{mol})$
LOX	(O_2)	Cryogenic	-183	1.149	-3.1
Ozone	(O_3)	Cryogenic	-112	1.614	+30.9
NOS	(N_2O)	Cryogenic	-88	1.226	+15.5
NTO	(N_2O_4)	Storable	+21	1.449	+2.3
RFNA	(HNO_3)	Storable	+80 to +120	1.583	-41.0
Peroxide	(H_2O_2)	Storable	+150	1.463	-44.8

LOX is a widely used oxidizer and burns with a bright yellow flame with most hydro-

carbon fuels. It has high attainable performance and is a commonly used oxidizer for large launch vehicles [6]. Although LOX is non-toxic and non-corrosive, it has other qualities that are much more undesirable. Because it boils at such a low temperature, well-insulated storage tanks, pipes, and valves must be used to eliminate any boiling losses during plumbing. This drastically increases storage and maintenance costs due to having to store it at such a low temperature. This also requires personnel with advanced training to ensure no one is harmed during the process as cryogenic LOX can cause severe frostbite.

NOS, also known as laughing gas, is a less potent oxidizer than the majority listed in Table 5, but still facilitates combustion at raised temperatures. Although its liquid temperature range is exceedingly small, it is self-pressurizing which eliminates the need for separate pressurization tanks. Combining that with its basic storage requirements and applicable performance, this makes NOS a very attractive oxidizer in low-cost scenarios.

NTO is a high-density liquid that is the most common very storable oxidizer today. It is mildly corrosive when pure but forms extraordinarily strong acids whenever exposed to water. It is also very toxic during its decomposition process. Because of its high vapor pressure, it must be stored in large tanks with compatible materials [6]. Although this oxidizer permits solid performance, it is dangerous to employ.

RFNA stands for red fuming nitric acid and was used during the mid-1900s. Specific types of stainless steel, gold, and other materials are required for storage of RFNA due to its high corrosiveness. When exposed to air, its fumes are poisonous. Other oxidizers today are more desirable.

Hydrogen Peroxide is a powerful liquid oxidizer that also permits clean burning. Its organic compounds are non-toxic when exhausted. When used as an oxidizer, its high concentrations cause severe skin reactions and can ignite when in contact with wood, oils, and other organic compounds [6]. Although this oxidizer shows promise, it has not been employed much in the United States due to its unpredictable storability.

The oxidizer chosen for this study was NOS. It has favorable combustion characteristics

and is non-toxic, non-corrosive, and has a desirable density and vapor pressure [28]. NOS has flown in space since the early 2000s with SS1, showing promise in HRE applications.

2.6.3 Additives

Additives perform many functions, including but not limited to shortening or lengthening curing times, improving rheological properties or physical properties, changing the transparency of to prevent radiation heating, or modifying chemical or physical reactions that occur during the burn [6]. Although there will be no comparison of additives in this study, it is important to note their ubiquity in hybrid rocketry, and rocketry in general. In HREs, additives are used to enhance performance characteristics of the fuel grain, or ease storage and handling requirements of potentially dangerous oxidizers.

The use of metal particles in hybrid fuel grains has been pivotal in increasing performance of HREs. By adding metal particles of various sizes to fuel grains, fuel regression rate, combustion efficiency, and motor stability can be modified to better fit the mission statement. Test firings performed by researchers from Naples, Italy [29] show that metal particles such as aluminium, magnesium, and iron increase regression rate by nearly 50%. This is due to the additives reducing the heat of gasification of the bulk fuel and the blocking effect induced by mass blowing. Metal and metal hydride powders raise the flame temperature and radiation feedback from the combustion products.

The use of additive-manufactured fuel allows for a seamless addition of metal powders whenever desired. It is common for FDM filaments to contain metal additives for aesthetic purposes, but for HRE applications, these additives give a boost in performance. There are also machines that can melt, extrude, and wind pellets of FDM filament to allow for the use of customizable filament. An external hopper is filled with the desired FDM filament pellets along with any metal additives that may be considered. The pellets are then fed into a heated extrusion chamber where they are subsequently melted and mixed. That mixture is then pushed out a small opening and rapidly cooled by external fans to create usable FDM

filament. An example of this apparatus can be seen in Figure 16.

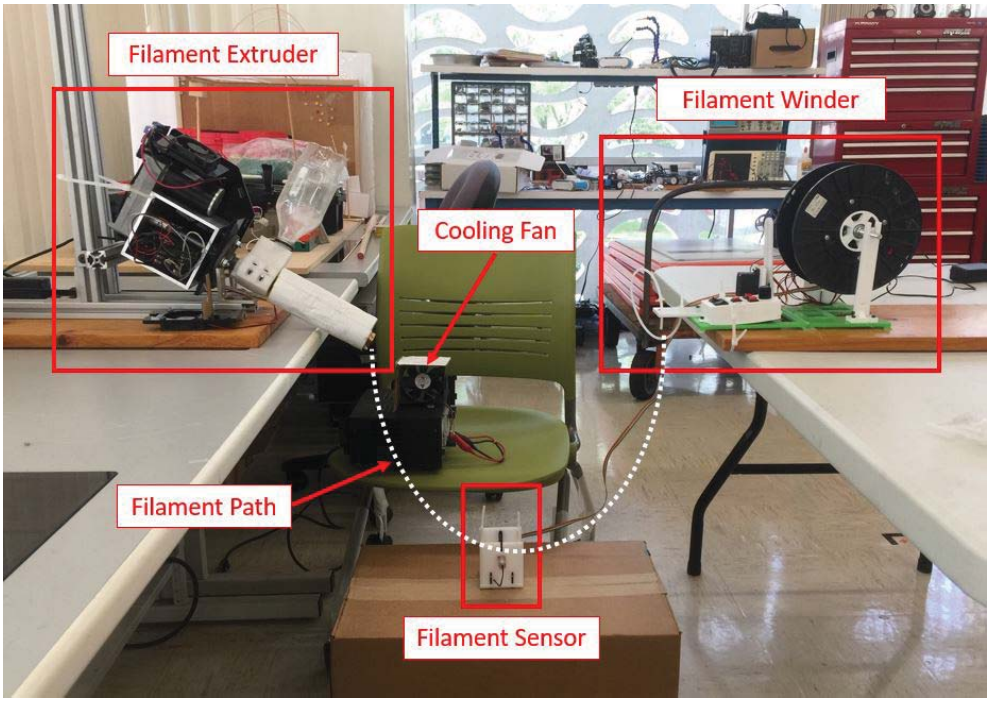

Figure 16: Filastruder Production Setup. [30]

As stated previously, no additives will be included in this study. However, to facilitate reliable combustion, a pyrogenic igniter will be used. Pyrogenic igniters utilize a small amount of propellant attached to the end of a wire. A current is passed through the wire via a control relay causing the propellant to ignite. This provides a strong flame to ignite the oxidizer flow and begin combustion of the solid fuel. Different igniters are used in different factions of rocketry, but almost always present. An example of a pyrogenic igniter is shown in Figure 17.

2.7 Literature Review on Hybrid Rocket Engines

Although the implementation of HREs has been sparse until recently, studies have been conducted for over fifty years on their performance trends. More recently, researchers from all around the world have focused on improving regression rate behaviors that are inherent in HREs, mostly by changing fuel types, fuel additives, and internal port geometries.

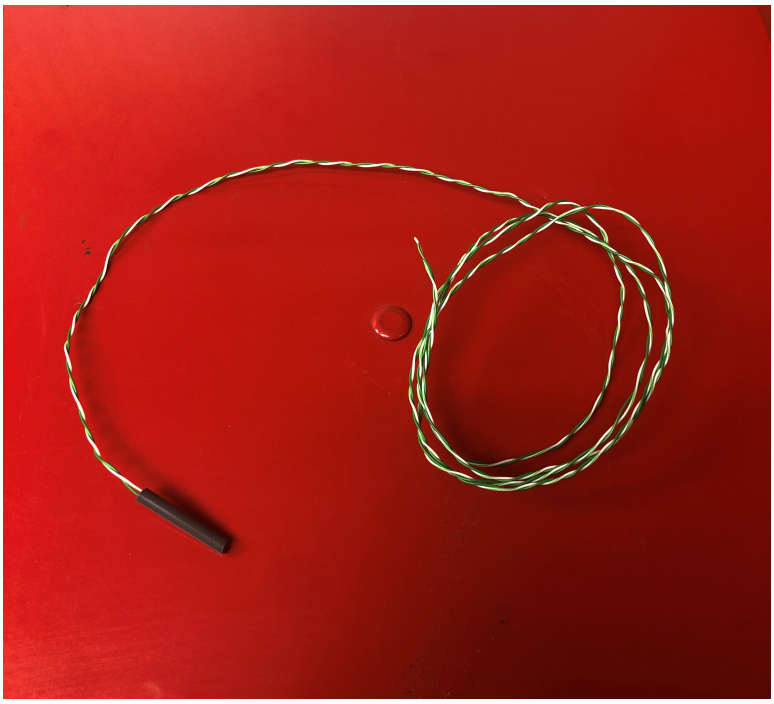

Figure 17: Pyrogenic Igniter.

Kevin Lohner et al. [31] performed a regression rate study on traditional and novel HRE fuels in a laboratory scale nitrous oxide hybrid propulsion system. The four HRE fuels tested include HTPB, high-density polyethylene (HDPE), polymethyl methacrylate (PMMA), and sorbitol. The scale explored in this work was a 2-inch (54mm) casing, scaled for one hundred pounds of thrust. Forty hot fire tests were performed to characterize the burn rates of fuels over a range of oxidizer flow rates, O/F ratios, and chamber pressures. This study characterizes the burn characteristics of hybrid rocket fuels with nitrous oxide as an oxidizer. Figure 18 shows the curves obtained by their experimental data.

Stephen Whitmore et al. [19] evaluated ABS as a potential fuel for HREs and compared it to the widely used HTPB, with nitrous oxide used as oxidizer. Analytical predictions for formation, products of combustion, and motor performance were compared against static fire tests for ABS fuel grains. Chemistry and performance of the ABS fuel grains are compared against fuel grains cast from HTPB of equivalent physical volume and dimensions. Tests were conducted using 98-mm motors for both ABS and HTPB. The ABS fuel grains were

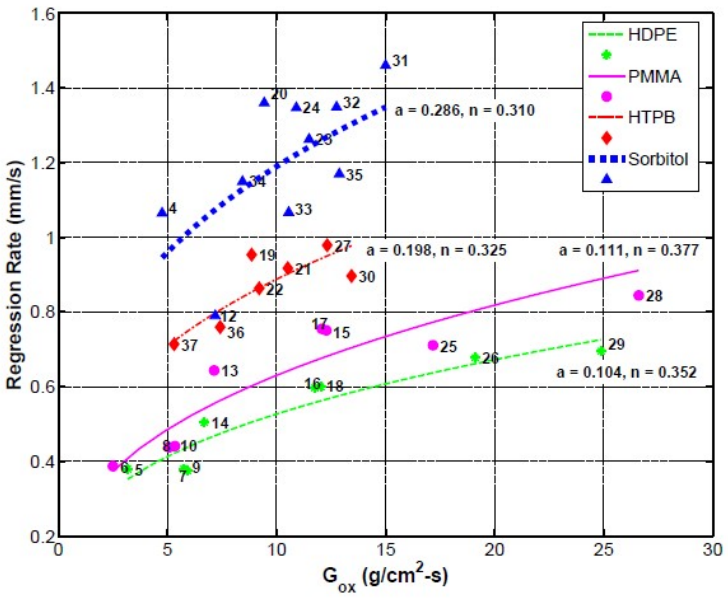

Figure 18: Regression Rate Curves Obtained Using Least Squares Fit of all Tests Performed. [31]

manufactured using direct digital manufacturing, now known as additive manufacturing, or 3-D printing. Twenty successful separate static fire tests including six ABS and fourteen HTPB fuel grains were performed. However, data from several of the tests were discounted due to known instrumentation, software, and test apparatus difficulties. The presented time history profiles include thrust, total impulse, injector and chamber pressures, and oxidizer mass flow. For each case, HTPB exhibited a small but well-defined advantage in overall performance, including thrust, total impulse, and specific impulse. HTPB outperformed ABS in thrust and impulse by 4.9% and 6.6%, respectively. Although HTPB offered better overall performance, ABS offered a slightly greater run-to-run consistency, with an average standard deviation of ± 17.2 N, compared to ± 32.2 N for its HTPB counterpart. This is likely due in part to the fabrication process of the ABS grains. This serves as one of the pioneering experiments when discussing ABS as a potential alternative to HTPB in HREs.

Stephen Whitmore et al. [12] continued his study of regression rates with a development campaign where modern additive manufacturing methods are used to fabricate HRE fuel

grains with embedded helical ports. The experiments featured ABS and gaseous oxygen as the oxidizer. Helical port structures, enabled through AM, increase the volumetric efficiency of the fuel grain by lengthening the internal flow path for a given port length. Sixteen static test firings were performed measuring the time histories of thrust and chamber pressure. The results of this experiment demonstrate that the centrifugal flow patterns introduced by the helical port structures increases fuel regression rates significantly. Mean regression rates as a function of oxidizer mass flux were increased by greater than four for the aggressive helical port structures, and greater than 2 for the modest port structures. Figure 19 shows a representation of the helical port structures described.

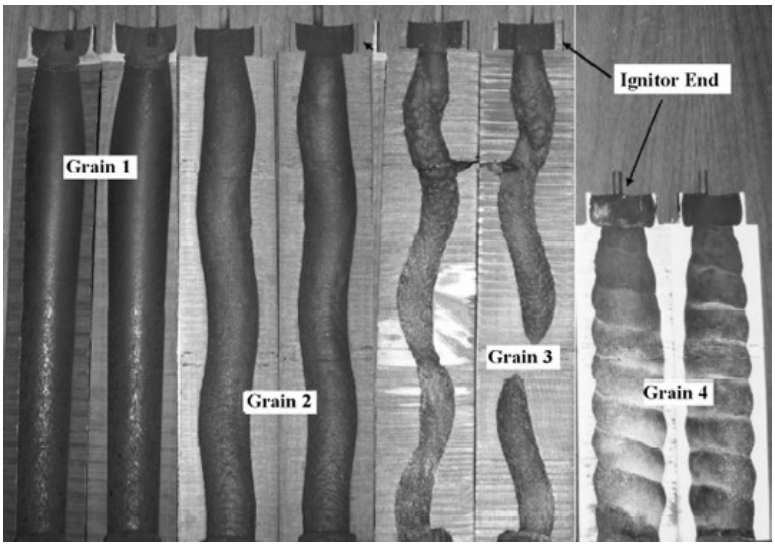

Figure 19: Helical Fuel Port Cross Sections. [12]

Xiaodong Yu et al. [32] performed a study on the mechanism and combustion performance based on fuel packing density of ABS. Grid-like structure fuels with different packing densities were prepared to assess performance characteristics of penetrative combustion. Fuel grains with packing densities ranging between 60% and 100% were testing across five separate burning times in a hybrid 2-D radial burner. The results of this study show that, compared with solid grains, the regression rates of 3-D printed ABS fuel grains increase to different degrees under the influence of penetrative combustion. Yu notes challenges remain to be addressed in future work, including deeper studies on the effect of this penetrative combus-

tion mechanism, extensive analysis of other materials, quantitative evaluations of the critical density, and more complex internal structural design. Figure 20 shows the combustion of the test specimens.

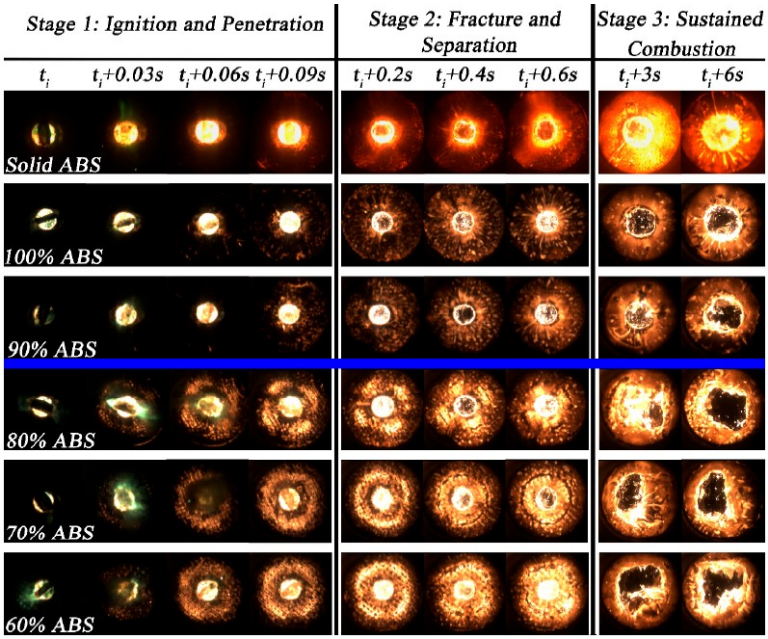

Figure 20: Combustion Histories of ABS Grains with Different Packing Densities. [32]

Mitchell McFarland et al. [18] performed small-scale static fire tests of 3-D printed fuel grains produced from varied materials for an HRE. Their material selection was based on commercially available filaments including ABS, ASA, PLA, PETG, Nylon, and PP. Tests were conducted in a 38-mm motor configuration. ABS and ASA were shown to have the best burning rate by inspection. A regression rate model showed that ABS and PLA performed similarly, further validating that PLA can be used in a HRE setting. Although many AM filaments were considered, their infill density and geometry were set as control variables. Further studies varying infill density and infill geometry are needed to see their effect on regression rate of AM filament HRE fuels. Figure 21 shows a visual representation of the fuel grains.

Byeonguk Ahn et. al [22] ran a laboratory-scale hybrid propulsion system using PLA and hydrogen peroxide. Hot fire testing was executed to investigate PLA as a potential fuel

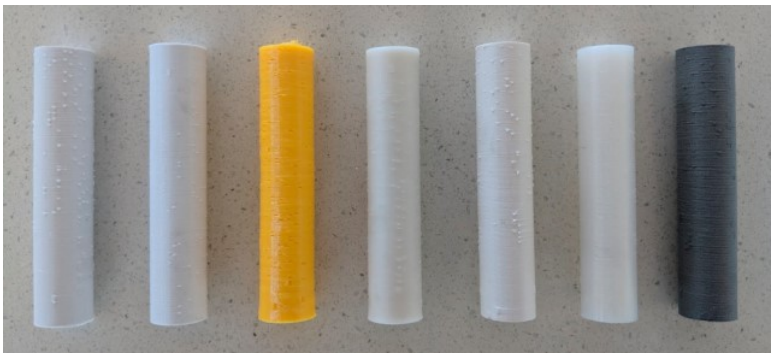

Figure 21: Small-scale fuel grains, left to right: ABS, PLA, PETG, PP, ASA, Nylon, and PLA with AL. [18]

in HRE applications. The estimated specific impulse of PLA in conjunction with hydrogen peroxide was about 223 s, just slightly lower than HDPE. These hot fire results validate that PLA can be used as an alternative material for the solid fuel grain in an HRE. PLA was also shown to be optimal at a lower O/F ratio range, 3.0 compared to 7.8 with HDPE. Although the specific impulse was lower with PLA, this implies that a much more compact oxidizer tank design may be available for PLA fuel HREs. PLA exhibits a higher mean mass flow rate and higher characteristic velocity efficiency.

2.8 Theory of Analysis

This study focuses on six different rocket performance parameters and their statistical variations. These parameters consist of mass flow rate, peak thrust, average thrust, total impulse, specific impulse, and regression rate. Three variations of solid fuel infill density and three variations of infill geometry were chosen to evaluate their performance variations. Initially, three different infill densities, 30%, 50%, and 70%, are varied in a cubic infill geometry. Subsequently, two different infill geometries, triangular and concentric, are varied with a infill density of 50%. Each different configuration consists of five separate tests to ensure all assumptions made based on this testing campaign are accurate and well developed. All five solid fuel configurations are evaluated on an HRE thrust stand in a 38-mm (1.5in) casing

with a total solid fuel length of 3.5 inches. Thrust is recorded as a function of time for all tests, whereas total impulse and specific impulse are calculated based on the burn characteristics such as burn time and mass flow rate. Oxidizer mass flow rate is calculated using mass flow parameter of NOS at conditions created in this testing campaign, and physically verified by weighing the testing bottle before and after hot firings. Fuel grains are weighed before and after each hot fire test to physically track the fuel mass flow rate. Regression rate is calculated analytically based on the weight of the fuel before and after firing using equations characterized by Marxman et al. [8, 9, 10] and further expanded by Whitmore et al. [12]. Regression rate is physically examined by cutting and measuring the difference in port geometry diameter after each test to determine the actual fuel regression rate. Nozzle geometry is determined with preliminary tests to assess the most consistent results.

CHAPTER III

EXPERIMENTAL METHODOLOGY

3.1 Fuel Grain Manufacturing

As stated previously in section 2.6.1, most HRE solid fuels are manufactured through the cast and cure method. Although most of the traditional HRE fuels are highly energetic, this manufacturing method leaves little room for complex geometric design parameters such as non-uniform port geometry structures. Cast and cure manufacturing is also very labor intensive, requires an exact ingredient mixture to ensure proper fuel formation, and can release harmful gases if not protected properly. The use of AM to print solid fuel grains alleviates all those problems with a passive manufacturing method that produces tight tolerances and complex internal geometries.

3.1.1 Design

To test an HRE, the process begins with designing and manufacturing solid propellant. In this study, 3-D printed PLA will be the fuel of choice due to its validity of a solid propellant in an HRE system, cost-effectiveness, and lack of health concerns associated with its manufacturing and storage. White Build Series PLA from MatterHackers will be the PLA used during this study, along with a Creality Ender 5 3-D printer. To design and manufacture 3-D printed PLA, CAD software must be used to interface between the designer and printer to ensure the part gets designed correctly. The CAD software used to execute the fuel grain design is SOLIDWORKS, a common and robust CAD software utilized in academia and industry alike.

Solid fuel grains have a range of different core geometries that correspond to different thrust profiles. Figure 22 depicts the relationship between solid grain port geometries and their thrust curves, respectively.

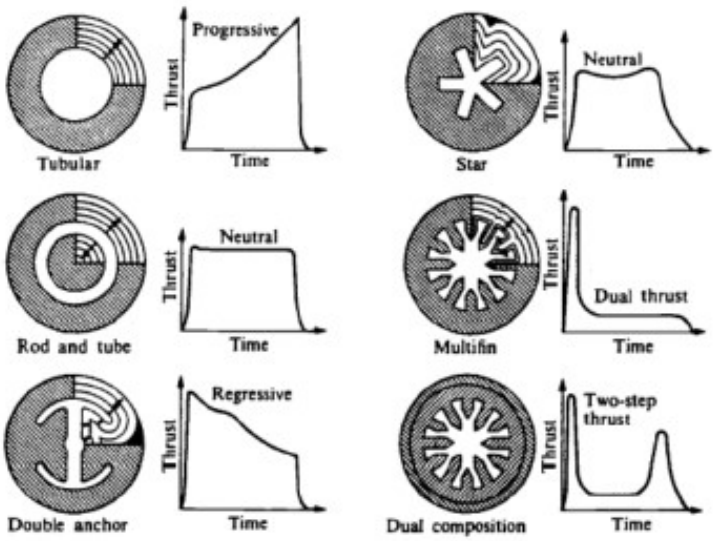

Figure 22: Common Solid Fuel Port Geometries and Their Respective Thrust Curves. [4]

Due to simplicity and past benchmarking, a port geometry known as Bates grain was selected. Bates grain, or tubular if referring to Figure 22, is the stereotypical port geometry choice due to its favorable chamber pressure and thrust curve. Bates grain geometry is characterized by a long cylindrical shape. Initial designs for this fuel grain correspond with a 38-mm diameter to fit snugly inside the motor casing, along with a port diameter of 0.65-in and an overall length of 3.5 in. Figure 23 shows a rendering of the fuel grain modeled in SOLIDWORKS.

Bates grain is a common port geometry in solid rocket motors due to simplicity and performance. Its practice in HRE applications is much less trivial, however. Due to the combination of oxidizer flow and pyrogenic igniters, preliminary tests showed difficulty with keeping the igniter in place within the fuel grain to facilitate reliable combustion. As the NOS flows at a high pressure, it wants to eject the igniter out the back of the casing, rendering it useless and resulting in a failed test. Thus, adjustments to the fuel grain were made to

Figure 23: Fuel Grain Design.

allow the igniter to remain in contact with the fuel grain during the duration of the burn period. An igniter holder was designed inside the Bates grain geometry; a six-fin seat for the igniter that acts as a small cavity for the igniter to lodge itself in, while also promoting initial mixing and adding turbulence to the flow for better combustion characteristics. Figure 24 shows a magnified rendering of the igniter holder within the port of the fuel grain.

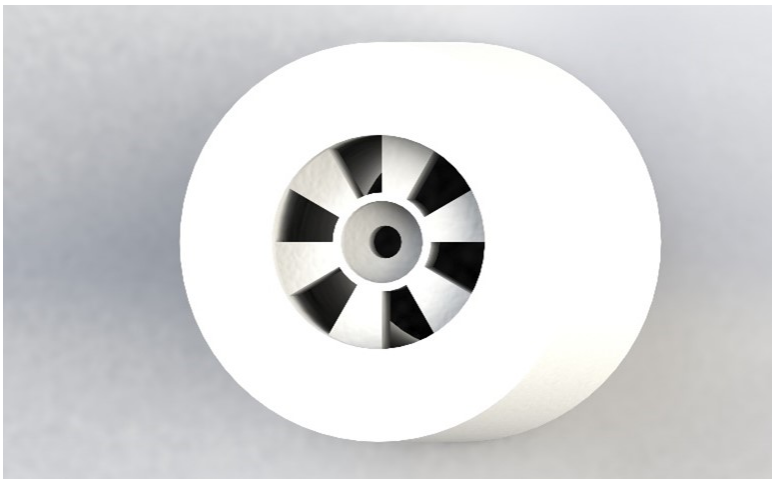

Figure 24: New Fuel Grain Design with Igniter Holder.

Preliminary testing proved the effectiveness of the igniter holder and this fuel grain port geometry.

3.1.2 Slicing

After being designed in the CAD software, the fuel grain must be prepared for transmission to the Ender 5 printer. This is accomplished by saving the SOLIDWORKS file as a Standard Tessellation Language (.STL) file. This converts the CAD part into a tesseract of triangular shapes to interface itself with the printer's software. However, before it can be sent to the printer, it must be run through slicing software to give the new .STL file parameters by which it is printed. The slicing software used for this study was Cura. In Cura, parameters outlined in Table 2 can be altered to further customize the way the part is printed. Many of these settings were left in their default state, while others were critical design parameters of this study.

The first design parameter altered is known as infill density, or infill percentage. Whenever a print is executed, the printer goes through a series of commands to save filament while also making the part as structurally sound as possible. This involves the printer to execute a complex series of algorithms that result in solid wall layers on the outside and a matrix of filament on the inside of the part. While the wall layers have a 100% infill density, the matrix is specified based on the user's needs. It is a well-known phenomenon that surface area and volume play an integral role in the rate at which fuel is burned inside any type of rocket engine or motor. To understand the role different surface areas and volumes can make, the infill density of the fuel grain prints was varied in Cura between 30, 50, and 70%.

Another design parameter altered is known as infill geometry, or infill shape. Not to be confused with port geometry mentioned in section 3.1.1, infill geometry specifies the shape of the matrix that constructs the part between its wall layers. Cura has many different infill geometries, each with its own practical use such as rigidity, strength, or flexibility whenever needed. A very standard geometry known as cubic was used as the baseline for testing in this study. All three sets of varying infill percentages were printed with cubic infill geometry, as this is what Cura initially recommends due to its strong structural properties. To further understand the role of these manufacturing parameters and their relationship with regression

rates in HRE fuels, two other infill geometries were chosen at a constant infill density of 50%. These two new geometries are known as triangular prism and concentric. As the shapes of the infill changes, so do the amount of filament, surface area for burning, and volume inside the internal matrix of the print. These changes represent key tuning parameters for the rate burning of the solid fuel. Figure 25 shows a representation of the different infill densities and infill geometries used in this study.

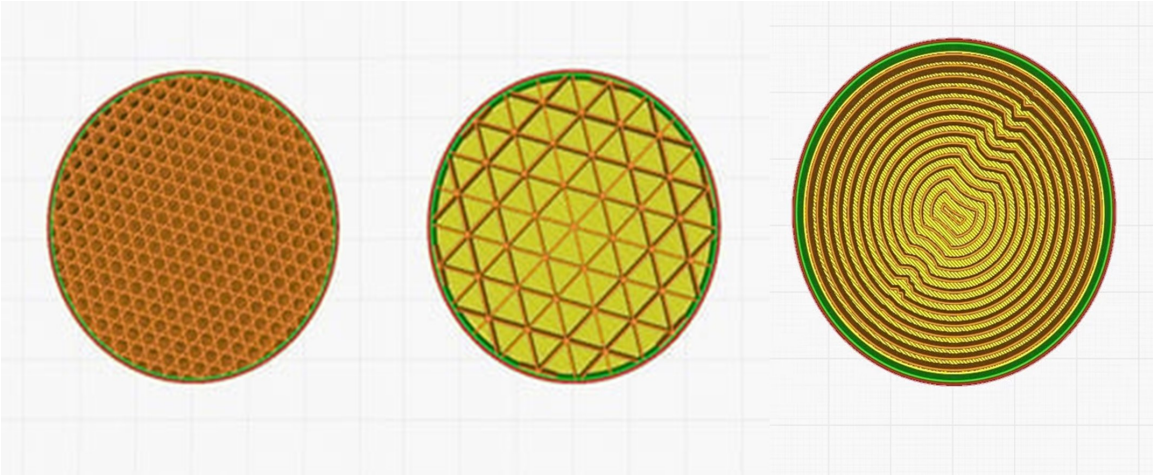

Figure 25: 50% Cubic (left), 20% Triangular (center), and 25% Concentric (right).

Most of the other values received little to no alterations during this study. The PLA was printed at its recommended print speed, nozzle temperature, and bed temperature to ensure proper heating and adhesion to the bed during the print process. Once all the parameters are adjusted, Cura will slice the part and save it as a file that interfaces with the Ender 5 printer.

3.1.3 Printing

To print the part with accuracy and precision, a few pre-print readiness checks must take place. The most important part of a 3-D print is ensuring the build plate is level. While some printers have digital bed leveling capabilities, the Ender 5 is mechanically leveled. There are small screws on the corners of the build plate that can be twisted to move that portion of the build plate up or down according to where the nozzle is located. A common leveling method

is to take a sheet of paper and manipulate it underneath the nozzle and on top of the build plate until the sheet is touching both the nozzle and plate but slides freely with little to no friction between the two. This ensures that the nozzle is close enough to the build plate for proper adhesion but does not interfere with itself or the print as the molten filament leaves the nozzle. The printer is then set to go through a process of preheating the nozzle and print bed to ensure the filament will flow smoothly and properly adhere to the build plate. This also helps remove any filament that was stuck in the nozzle or extruder from past prints. Once the build plate is level, and the printer has been pre-heated, the print can take place. Table 6 shows the different print configurations and their print durations.

Table 6: Print Time and Print Weight of Fuel Grain Configurations.

Infill Density (%)	Infill Geometry	Print Time (hrs:min)	Print Weight (Grams)
30	Cubic	3:22	30
50	Cubic	4:20	42
70	Cubic	5:09	53
50	Concentric	2:55	38
50	Triangular	4:43	42

3.2 Oxidizer Transfer and Utilization

To test an HRE in a safe environment, special care must be taken in order to ensure the fuel and oxidizer are used properly during testing, handling, and storage. Since the fuel used in this study is PLA, the handling requirements are minimal. On the other hand, NOS is a highly compressed gas that boils at ambient conditions and requires attention when used. To mitigate risk, most of the NOS is stored in a mother bottle that is stored inside Richmond Hill Research Complex in the Rocket Advanced Manufacturing (RAM) Lab. During test firings, NOS is transferred from the mother bottle to a smaller testing bottle via a NOS refill

station inside the RAM Lab.

3.2.1 Test Bottle

To safely and easily test on a portable HRE stand, a small and portable 10-lb bottle of NOS was included. A 10-lb testing bottle was deemed the right fit due to its size, reasonable price point, and safety. The 10-lb bottle provided a medium point between good pressure capabilities of the bottle while still holding enough to support more than just a few tests between refills. A visual representation of the steel-walled testing bottle can be seen below in Figure 26.

Figure 26: 10-lb NOS Testing Bottle.

3.2.2 Refill Station

A NOS refill station was implemented to safely transfer NOS from the mother bottle to the testing bottle. This consists of a large 50-lb mother bottle of NOS, a centrifugal pump, a shut off valve, nitrous filter, scale, and necessary hoses and fittings. To safely and promptly refill the testing bottle, special adjustments were made to the mother bottle. These adjustments include implementing a bottle warmer and inverted bottle-holding stand. A bottle warmer is an electric heated blanket that wraps around the mother bottle to energize the NOS inside the mother bottle, which increases the bottle temperature. This allows the NOS to flow more quickly between bottles. The inverted stand accomplishes the same action by taking advantage of gravity. The stand screws into the top of the mother bottle, allowing it to be balanced on its head so gravity will assist in pushing NOS from the larger bottle to the smaller bottle. It is common practice to also cool the receiving bottle while warming the mother bottle. During refill sessions, the testing bottle is kept in an ice bath to keep its internal pressure low, so it wants to receive the NOS flowing from the mother bottle. A visual representation of the NOS refill station can be seen in Figure 27.

Certain procedures must be followed to ensure the testing bottle is properly filled and no waste is accumulated. The procedures are as follows:

1. Plug in and turn on the bottle warmer. Let sit for a few minutes.
2. Turn on and tare the scale.
3. While the scale is initializing, make sure the turn valve is closed and open the mother bottle.
4. Ensure the testing bottle is closed, then set the testing bottle on the scale and record its current weight.
5. Attach the fill hose to the testing bottle nipple and tighten to a secure fit, then slowly open the turn valve. This will push all the NOS to the testing bottle nipple.

Figure 27: NOS Refill Station.

6. Slightly loosen the fill hose at the testing bottle nipple to bleed excess air out of the line. This will ensure the testing bottle does not get contaminated during filling. You will know all air has escaped whenever you see NOS escaping the hose.

7. The side of the testing bottle shows the bottle weight, the weight of NOS it can hold, and their total combined weight. Take the result of step 4 and subtract it from the total weight of the bottle and gas. This will give you the empty weight remaining in the bottle.

8. Zero the scale again and open the testing bottle to allow for the flow of NOS between bottles. If the testing bottle is cold, you may not have to run the pump to fill the

bottle. If the bottles are the same temperature, you may need to run compressed air through the pump-to-pump NOS from bottle to bottle.

9. Verify the testing bottle is completely filled by reaching the weight calculated in the previous step.

3.3 Experimental Setup

To accurately predict and simulate combustion effects in an HRE, a static thrust stand must be used. Thrust stands for rocket engines vary from tabletop size to filling thousands of feet of space. Due to the scale of this testing campaign, a tabletop-sized thrust stand is capable of fulfilling the needs required by the HRE.

3.3.1 HRE Test Stand

The base of the stand is a rectangular steel table that sits on casters. These casters can be locked and unlocked to allow for the table to be easily movable and stable. This table also has area underneath where benches are mounted to include the necessary mounting pieces for the oxidizer feed system. A SOLIDWORKS representation of the table without the oxidizer feed system is shown in Figure 28.

The thrust stand used in this study implements an HRE that nests inside aluminium plates supported by threaded rods. This sled creates room for oxidizer feed and necessary plumbing, so the load created by the HRE does not affect oxidizer flow. These aluminium plates interface with the thrust ring on the casing while also supporting the casing itself to allow for better momentum transfer to the thrust post, and ultimately, the load cell. This sled created by the aluminium plates and threaded rods are interfaced into linear bearings that allow for accurate transmission of thrust through t-slot aluminium that has been rigidly attached to a mobile stand. A visual representation of the HRE sled can be seen in Figure 29.

Figure 28: Test Stand Table Structure.

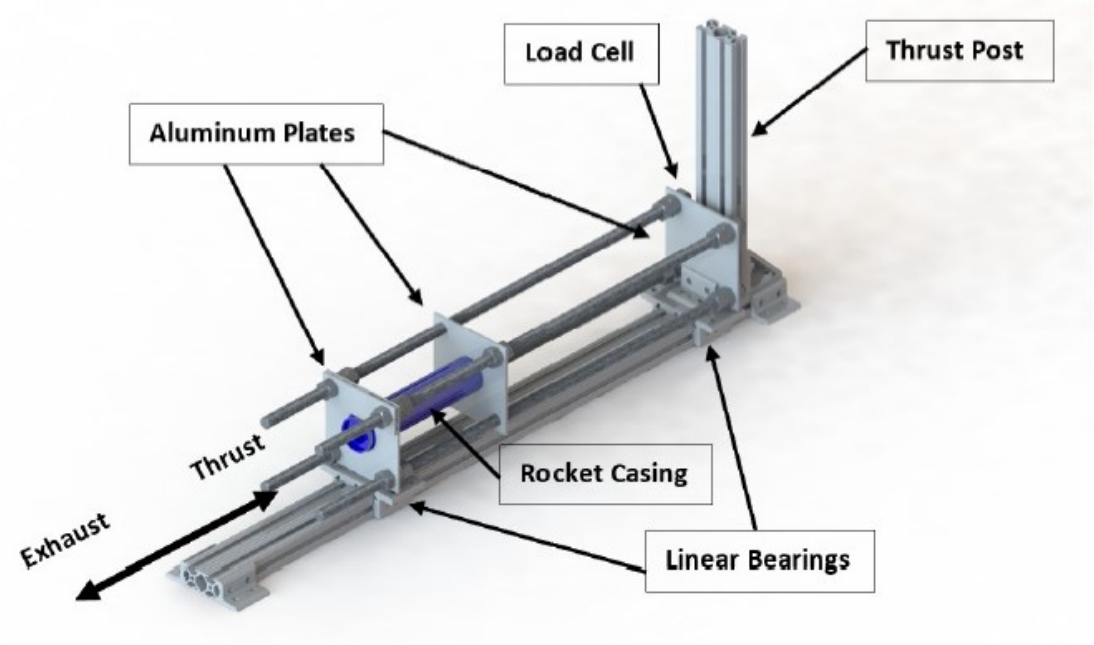

Figure 29: Test Stand Sled Structure.

3.3.2 Oxidizer Delivery System

The oxidizer delivery system allows to safely transport the oxidizer from the testing bottle to the thrust chamber. This delivery system implements the 10-lb testing bottle, mounting clamps, braided hose, pressure regulator, solenoid valve, orifice plate, and injector. NOS

is a self-pressuring gas due to its low boiling point and high vapor pressure. This allows for direct storage underneath the test stand without other needs of cooling or pressurizing. Table 7 shows the pressure of NOS at varying temperatures close to the ambient condition.

Table 7: NOS Temperature and Corresponding Pressure. [33]

Bottle Temperature ($^{\circ}F$)	Bottle Pressure (psi)
32	460
40	520
50	590
60	675
70	760
80	865
97	1069

The NOS flows directly to a pressure regulator, where the user regulates the output pressure of the bottle between 200-1100 psi. The ability to vary pressure allows for different mass flow rates of oxidizer on the same stand, which is an inherent plus for testing. In this study, a single oxidizer mass flow rate of 200 psi is used. Directly downstream of the pressure regulator sits the solenoid valve. This solenoid valve serves as the on/off switch for the oxidizer and is controlled via an electronic relay board.

Further downstream of the solenoid is the orifice plate. The goal of the orifice plate is to be able to meter the flow of oxidizer based on Mass Flow Parameter (MFP). The equation for MFP can be seen in Equation 3.3.1.

$$MFP = \frac{\dot{m} * \sqrt{T_t}}{A * P_t} \tag{3.3.1}$$

By using Equation 3.3.1, the mass flow rate of oxidizer can be obtained. Assuming a set pressure by the pressure regulator and a temperature that matches that pressure for NOS,

the mass flow through the orifice can be adjusted based on the area of the orifice by assuming choked flow through the orifice. Choked flow refers to the velocity of the flow relative to the speed of sound, (a). The equation for a can be seen in Equation 3.3.2. The MFP parameter can be obtained through gas tables by knowing the ratio of specific heats, (γ), and molecular weight of the fluid, (MW).

$$a = \sqrt{\gamma * R * T} \tag{3.3.2}$$

After an iterative process, the orifice plate can be machined based on the hole diameter needed for the oxidizer flow selection. The final design of the orifice plate used for this study is shown in Figure 30. The orifice plate is sandwiched between two flanged fittings to restrict the flow to the orifice. Exceptional care was taken to design the orifice to the correct size for accurate oxidizer flow measurements. Many cold fire tests were conducted to ensure accurate measurements. In these cold flow tests, the oxidizer ran for a set amount of time, and weighed before and after the test. This allowed for calculation between actual mass flow and theoretical mass flow, which were closely correlated. Table 8 displays the parts used for the oxidizer delivery system as well as other necessary parts.

Table 8: HRE System Parts.

Part Type	Part Model
Test Bottle	Nitrous Outlet 10-lb
Braided Hose	6 AN
Pressure Regulator	Palmers Pursuit Air Pressure Pro
Solenoid Valve	Burkert 6027
Plumbing	1/4 NPT
Load Cell	Futek LLB400 500-lb
Power Supply	National Instruments PS-15
DAQ	National Instruments USB-6211

After moving through the orifice, the oxidizer is ready for the combustion chamber. Downstream of the orifice plate is the injector. The injector is what guides the flow into the combustion chamber. The injector used in this study axially injects the flow of NOS into the combustion chamber. This design choice was chosen for simplicity.

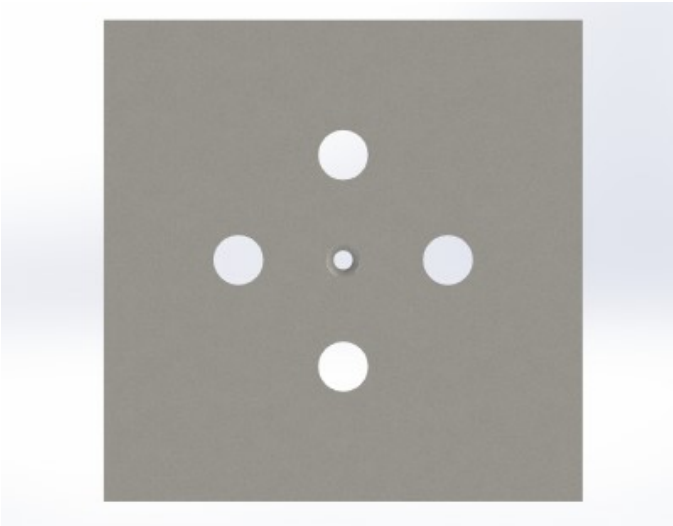

Figure 30: Orifice Plate Design.

3.4 HRE Hot Fire Testing

Before any hot fire tests can commence, a series of pre-test readiness checks must take place. These pre-test readiness exercises include prepping the solid fuel grains for integration into the thrust chamber, preparing the testing bottle for oxidizer flow, verifying the pressure of oxidizer in the feed system, assembling the rocket casing, stand integration, and configuration of the LabVIEW Virtual Instrument (VI). Each of these steps are pivotal in the functioning of the hybrid thrust stand and must be executed with precision and care for a reliable and safe testing environment.

3.4.1 Solid Fuel Preparation

After the solid fuel grains are designed, sliced, and printed, the fuel grains must be prepared for integration with the thrust chamber and testing. It is good practice within rocketry to use

liners within the thrust chamber to ensure the casing is not exposed to the high temperature ranges created by the fuel and oxidizer burning. Liners are usually comprised of paper or, in more extreme cases, phenolic material. Phenolic liners are made of alternating layers of cured resin and fibrous materials such as cotton, paper, or glass-based fabric. These materials are sandwiched under extreme pressure and heat forming a solid thermoplastic that has strong structural and thermal properties, ideal for rocket applications. To ensure the hot fire tests were as safe as possible, this study implemented phenolic liners as insulation between the solid fuel grain and casing. These liners were cut with precision and care to ensure a perfect integration within the rocket casing.

After cutting, a fit check must take place to mitigate risk of failures during hot fire testing. Fit checks consist of assembly of the rocket casing with all necessary parts including snap rings, nozzle washers, nozzle, fuel grain, liner, O-rings, injector, igniter, and snap rings. Figure 31 shows a visual representation of all necessary parts needed for the solid fuel preparation.

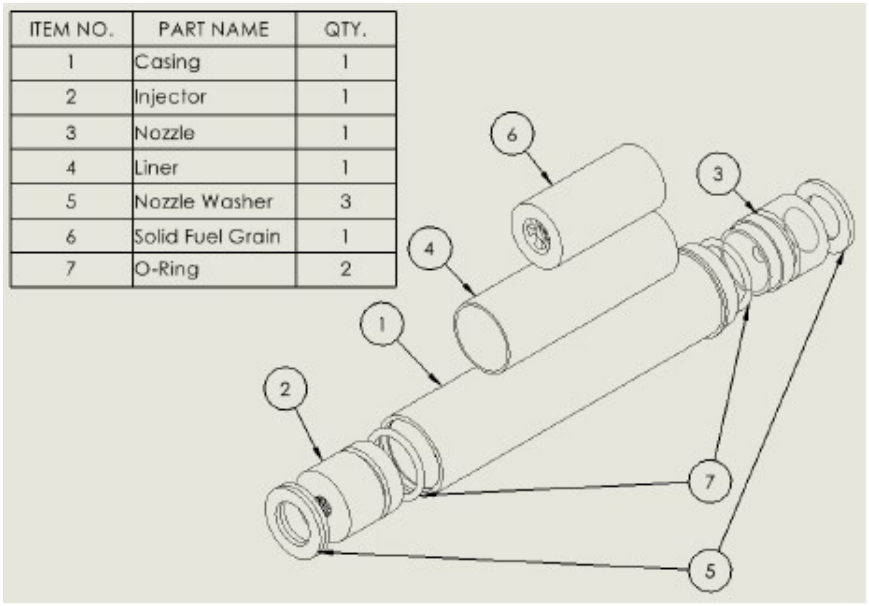

Figure 31: Exploded and Numbered View of Solid Fuel Assembly.

In this assembly, the injector acts as the forward closure of the thrust chamber and threads into the oxidizer feed system to allow for secure flow. The forward closure is sealed with a

small rubber disk called an O-ring that ensures no gas can escape the forward closure. The forward closure is secured into place with a snap ring. Directly downstream of the forward closure is the liner and fuel grain that interfaces directly with a converging-diverging nozzle that is sized during the initial tests of this campaign to ensure for the most reliable analysis of performance. The nozzle is also pressure sealed with an O-ring and is sandwiched with another snap ring to secure the other end of the thrust chamber. Figure 32 is a visual representation of the layers of the thrust chamber with the forward closure, fuel, liner, and nozzle included. After the fit check, the fuel grains are glued into the liner to ensure there is no movement of the fuel during the burn. This glue must be left to cure for at least six hours to allow for adequate time to dry and adhere to the liner.

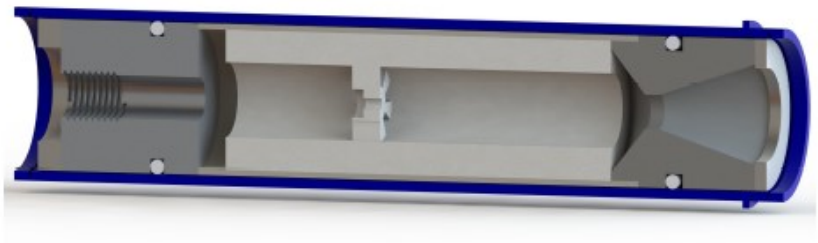

Figure 32: Section View of the Thrust Chamber Assembly.

3.4.2 Configuration and Instrumentation

Multiple different configurations must take place for the stand to perform as expected and accurately measure the thrust produced by the HRE. These configurations take place within the measurement system. The measurement system is split into the user interface, a measurement input, and two control outputs. A flow diagram of the inter-connectivity of the three groups is laid out in Figure 33.

A LabVIEW VI was integrated in order to simultaneously use the load cell, solenoid, and ignition into a single graphical user interface (GUI). The VI accomplished this by using a

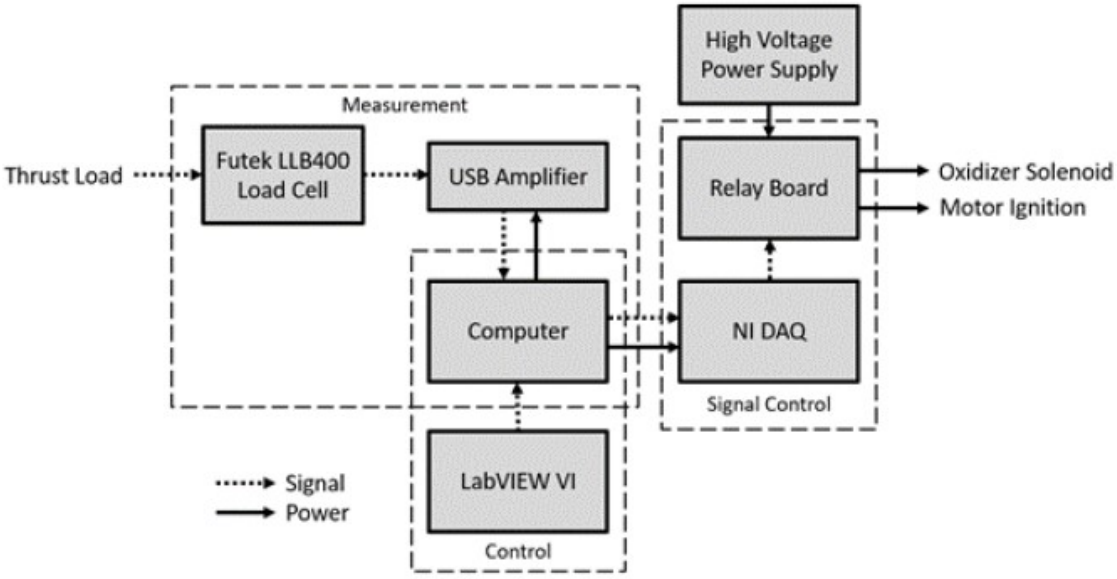

Figure 33: Flow Diagram for Measurement System.

Message Queue Handling architecture, where processes can take place in parallel while using independent loops. For controls, the DAQ is used for two signal outputs. These two signals interface with the relay board. When pulled high, these relays complete the circuit for either the oxidizer solenoid or igniter. The duration and timing offsets of these events are inputs within the LabVIEW GUI, allowing for sub-second timing. The LabVIEW GUI can be seen in Figure 34.

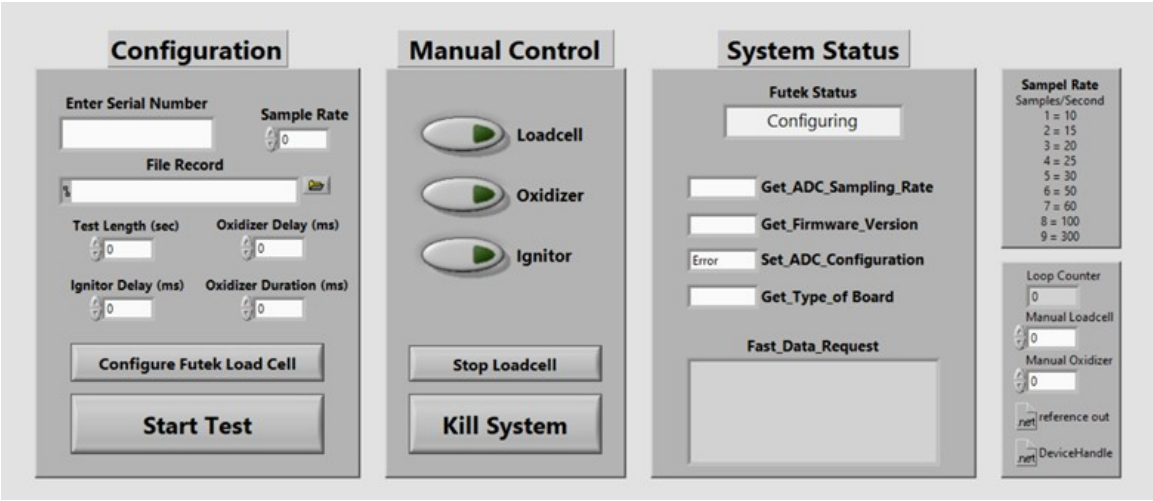

Figure 34: LabVIEW GUI Front Panel.

To be completely configured and ready for a test, the load cell must be calibrated and pre-loaded. A pulley system integrated into the steel table hangs pre-measured weights through the tables surface to make sure the load cell is receiving accurate data. Pre-loading the sled also keeps movement throughout the burn to a minimum. Calibrating the load cell was accomplished by using multiple different known weights to create a tight line of best fit for the data points.

3.4.3 Testing Procedures

Once everything is assembled in the rocket casing and all configuration of the instruments has been performed, the hot fire test can commence. Test procedures for this event are as follows:

1. Insert the igniter leads through the forward closure and nozzle until the igniter is seated in the igniter holder.
2. Use the aft aluminum plates to slide the combustion chamber into place.
3. Thread the combustion chamber onto the male fitting of the oxidizer feed system.
4. Apply 10-lb of pre-load to test stand load cell.
5. Tighten the thrust ring holder plate to the aft-most aluminum plate.
6. Connect the Futek USB and DAQ USB to the testing laptop and plug in the extension cord for the power supply.
7. Launch the LabVIEW VI and type in the load cell serial number and sampling rate, then choose a data output file location.
8. In the VI, set the total test length, oxidizer delay, igniter delay, and oxidizer duration.
9. Ensure the solenoid valve is closed and open the testing bottle valve. NOS can be heard going to the solenoid.

10. After the bottle is open, set the pressure regulator to the desired output pressure with a 3/16-in Allen wrench.

11. Take the installed igniter, strip the leads, and connect them to the test stand alligator clips. Be sure to touch alligator clips together before connecting the igniter leads to ensure that no voltage is being sent through the igniter during installation.

12. On the testing laptop, run the code for the VI. This will not start the test, but it allows the load cell to be configured.

13. Once the system status on the VI says "Configured", a countdown from 5 may begin and the "Start Test" button can be clicked.

14. Once the test has been completed, close the testing bottle and bleed the braided hose to ensure no ghost flames inside the combustion chamber.

15. Allow combustion chamber to cool to the touch before removing chamber from the test stand by loosening the bolts on the thrust ring holder and begin disposal of single-use parts.

CHAPTER IV

RESULTS

4.1 Preliminary Test Results

Preliminary tests were conducted to find the optimal nozzle performance for an inlet pressure of 200 psi and $\dot{m}_{ox}$ of 0.027 lb/s, with a burn time of 4 s. The nozzle sizes investigated in the preliminary tests were #13, #16, #19, and #25. The numbers refer to the diameter of their throats in inches as a fraction of 64. Figure 35 displays the thrust curves of these four different nozzle geometries as a function of time.

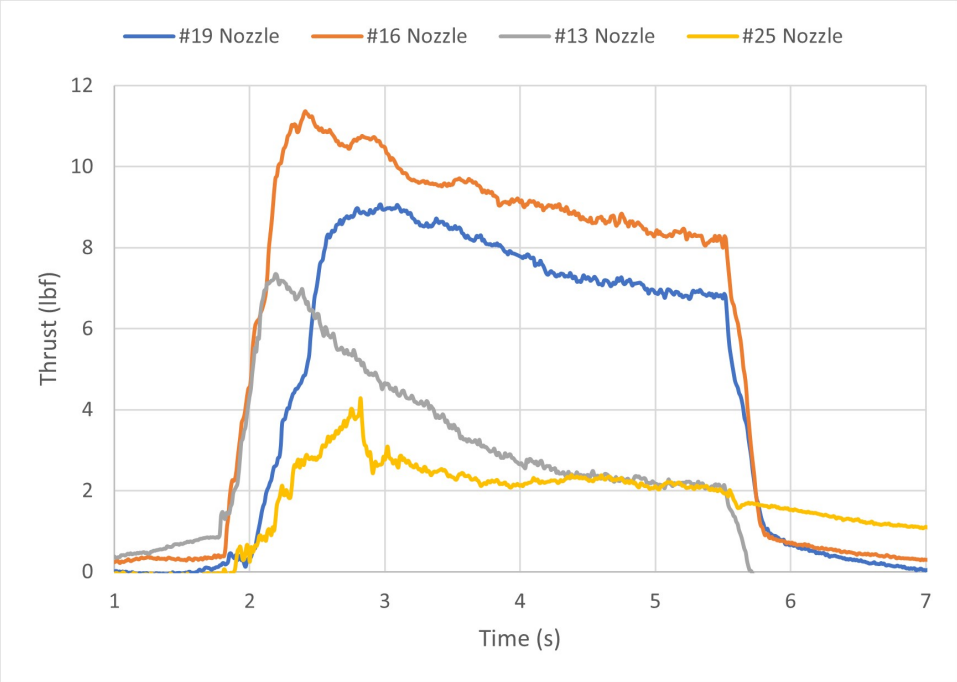

Figure 35: HRE Performance Based on Nozzle Size.

Each test begins with the opening of the solenoid valve near the 0.75-second mark and the rise in thrust due to ignition around the 1.75-second mark. All burns are considered

fairly neutral which is conventional of Bates grain geometry in HRE applications. Table 9 shows the peak thrust, average thrust, total impulse, and specific impulse for each nozzle configuration.

Table 9: HRE Performance Based on Nozzle Size.

Nozzle Size $\frac{\#}{64}(in)$	$F_{max}(lbf)$	$\bar{F}(lbf)$	$I(lbf * s)$	$I_{sp}(s)$
13	7.34	3.40	13.84	113.33
16	11.38	8.73	34.56	265.51
19	9.06	6.88	26.28	221.94
25	4.29	1.1	4.49	149.66

The process of deciding upon a nozzle was a combination of examining Figure 35 and Table 9. Nozzle #16 and #19 both performed well for this configuration of fuel and oxidizer. This can be seen by these tests reaching the best peak thrust and average thrust values while also having a neutral burn. The #13 nozzle likely did not allow enough mass flow out and caused the flame to snuff itself out due to over-pressurization. Conversely, the #25 nozzle likely did not accelerate the flow enough, not reaching mach 1 and could not produce aqeuate pressure within the chamber.

Slight variations in how the test stand was set up have occurred since the preliminary tests. Support braces for the solenoid and pressure regulator have been removed, which could account for a slight change in thrust measured. Manual quarter-turn valves were also added to prevent the unwanted flow of NOS into the combustion chamber, which could cause resonant burning within the fuel grain after the test has ended.

4.2 Test Results Overview

A twenty-five test hot fire campaign was carried out to determine the difference and variability of performance parameters related to the HRE system. In this section, thrust curves

related to fuel grains with differing infill densities and geometries will be displayed, as well as tables containing each hot fire test and their respective performance parameters.

4.2.1 30% Infill Density Cubic Infill Geometry

Figure 36 displays the thrust curve profiles against the burn time for the five tests completed with a 30% infill density and a cubic infill geometry. For this motor configuration, a unpredictable and violent rise and ignition period is followed by a consistent neutral burn profile. All ignitions tend to occur between 2.5 and 2.75 seconds with burn times between 5.25 and 5.5 seconds. Peak thrust values are created near the 3.0 second mark and vary widely between 4 and 10 lbf, while average thrust values stayed mostly constant around 3-4 lbf. Test 3 was left in the calculation, but could be considered an outlier based on its large peak and average thrust. All thrust measurements seem to converge near 4 lbf at the end of the burn period.

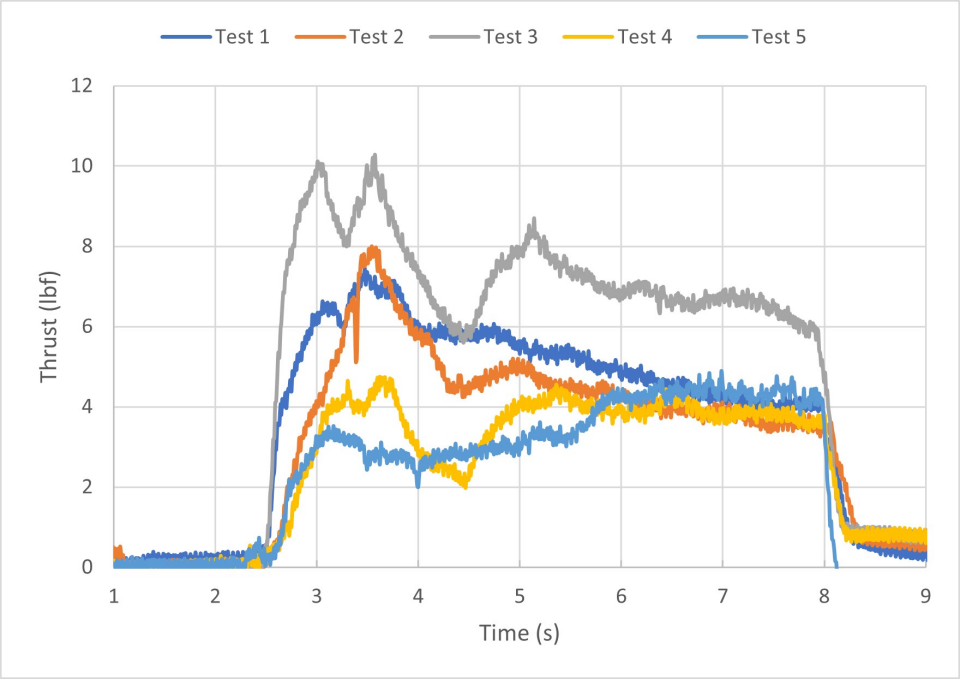

Figure 36: Thrust Versus Time for 30% Infill Density with Cubic Infill Geometry.

Table 10 displays the performance parameters for each hot fire test along with the average

and percent standard deviation from all tests of 30% density and cubic geometry. The average and percent standard deviations are calculated based on burn time calculations that result in the start and stop times being based on 10% of the peak thrust value. All performance parameters have a relatively high standard deviation across the burn other than regression rate, which remains approximately constant.

Table 10: Performance Parameter Results for 30% Infill Density with Cubic Infill Geometry.

Test Number	$F_{max}(lbf)$	$\bar{F}(lbf)$	$I(lbf * s)$	$I_{sp}(s)$	$\bar{r}(in/s)$
1	7.46	4.99	30.2	145	0.010
2	8.00	4.43	24.9	130	0.010
3	10.3	7.07	39.9	204	0.011
4	4.74	3.51	19.8	104	0.010
5	4.99	3.46	18.9	103	0.010
Average	7.09	4.69	26.7	137	0.010
% Std Dev	32%	31%	32%	30%	6%

4.2.2 50% Infill Density Cubic Infill Geometry

Figure 37 displays the thrust curve profiles against the burn time for the five tests completed with a 50% infill density and a cubic infill geometry. The trust curves created by this engine configuration feature a very neutral thrust profile with all rise times varying between 2.25 and 2.75 seconds with burn times of 5.25 to 5.75 seconds. Peak thrust of this fuel configuration vary across the burn time and vary between 7 to 10 lbf. Thrust measurements seem to converge around 7 lbf near the end of the burn.

Table 11 displays the performance parameters for each hot fire test along with the average and percent standard deviation from all tests of 50% density and cubic geometry. The average and percent standard deviations are calculated based on burn time calculations that result in the start and stop times being based on 10% of the peak thrust value. The performance

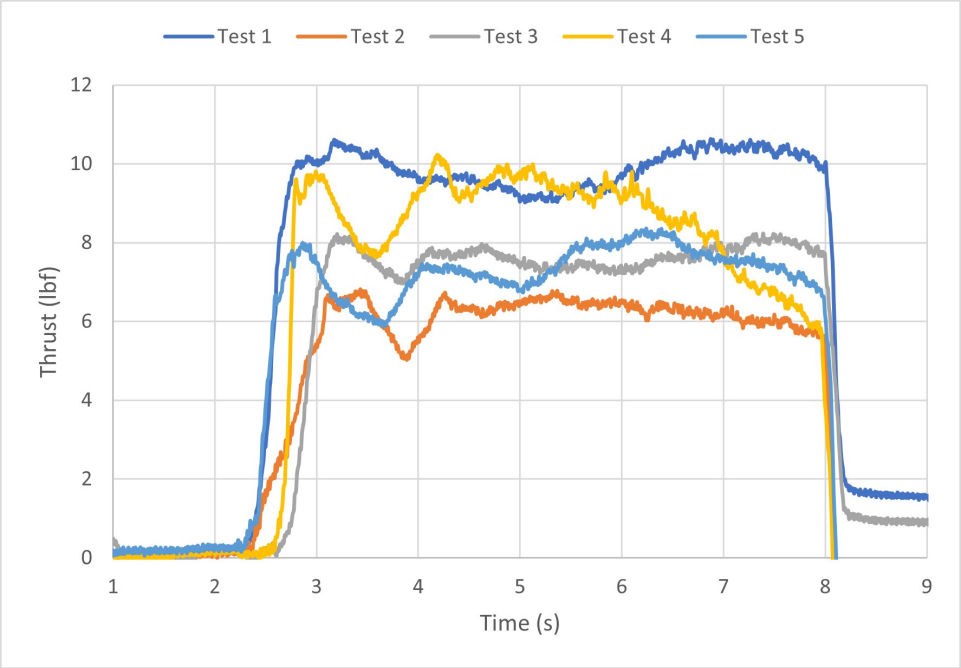

Figure 37: Thrust Versus Time for 50% Infill Density with Cubic Infill Geometry.

parameters of this section feature more consistency across the length of the burn with the regression rate being more variable in nature. Peak thrust is near 9 lbf while average thrust for this configuration was approximately 7.5 lbf. This results in the total impulse to be near 43 lbf*s for 50% infill density and cubic infill geometry.

4.2.3 70% Infill Density Cubic Infill Geometry

Figure 38 displays the thrust curve profiles against the burn time for the five tests completed with a 70% infill density and a cubic infill geometry. The trust curves created by this engine configuration feature a slightly regressive thrust profile with all rise times varying between 2.5 and 2.75 seconds with burn times of 5.5 to 5.75 seconds. Peak thrust of this fuel configuration tend to reside in the rise and ignition phase followed by consistent burns that average just over 6 lbf over the burn period. The thrust curves created by this fuel configuration are predictable in slope with peak thrust being near 8 lbf, while average thrust is near 6 lbf.

Table 12 displays the performance parameters for each hot fire test along with the average and percent standard deviation from all tests of 70% density and cubic geometry. The average

Table 11: Performance Parameter Results for 50% Infill Density with Cubic Infill Geometry.

Test Number	$F_{max}(lbf)$	$\bar{F}(lbf)$	$I(lbf * s)$	$I_{sp}(s)$	$\bar{\dot{r}}(in/s)$
1	10.63	9.50	54.8	288	0.008
2	6.82	5.41	30.7	160	0.009
3	8.24	7.27	39.9	222	0.008
4	10.22	8.34	45.5	236	0.011
5	8.36	7.09	40.5	211	0.009
Average	8.85	7.52	42.3	223	0.009
% Std Dev	18%	20%	21%	21%	14%

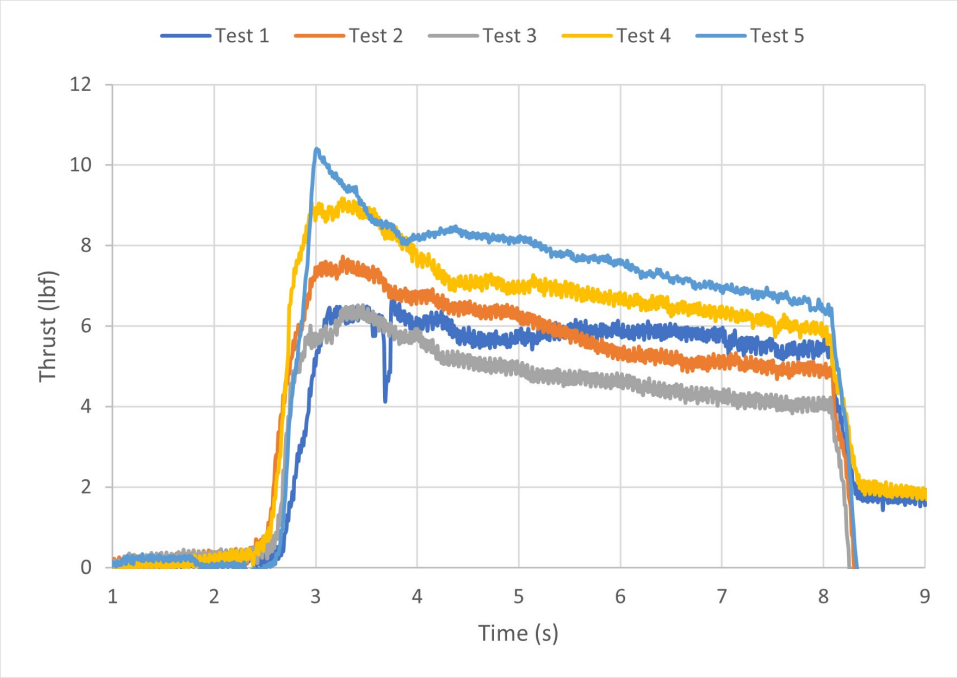

Figure 38: Thrust Versus Time for 70% Infill Density with Cubic Infill Geometry.

and percent standard deviations are calculated based on burn time calculations that result in the start and stop times being based on 10% of the peak thrust value. The percent standard deviations are nearly all 20% across the board with the regression rate being consistent at near 7%.

Table 12: Performance Parameter Results for 70% Infill Density with Cubic Infill Geometry.

Test Number	$F_{max}(lbf)$	$\bar{F}(lbf)$	$I(lbf * s)$	$I_{sp}(s)$	$\bar{\dot{r}}(in/s)$
1	6.72	5.64	32.2	181	0.006
2	7.73	5.59	33.3	179	0.006
3	6.52	4.69	21.35	159	0.006
4	9.16	7.44	43.6	238	0.006
5	10.4	7.45	42.1	233	0.007
Average	8.11	6.16	34.5	196	0.006
% Std Dev	20%	20%	26%	20%	7%

4.2.4 50% Infill Density Triangular Infill Geometry

Figure 39 displays the thrust curve profiles against the burn time for the five tests completed with a 50% infill density and a triangular infill geometry. Recall Figure 37 for reference as 50% density with a cubic geometry will be the basis of comparison for infill geometry study. The trust curves created by this engine configuration feature a high-rising ignition and rise phase followed by a very neutral burn profile. Peak thrust of this fuel configuration tend to reside in the rise and ignition phase followed by consistent burns that average approximately 6 lbf.

Table 13 displays the performance parameters for each hot fire test along with the average and percent standard deviation from all tests of 50% density and triangular geometry. The average and percent standard deviations are calculated based on burn time calculations that result in the start and stop times being based on 10% of the peak thrust value. Triangular infill geometry featured higher percent standard deviation across the performance parameter list than that of cubic infill geometry.

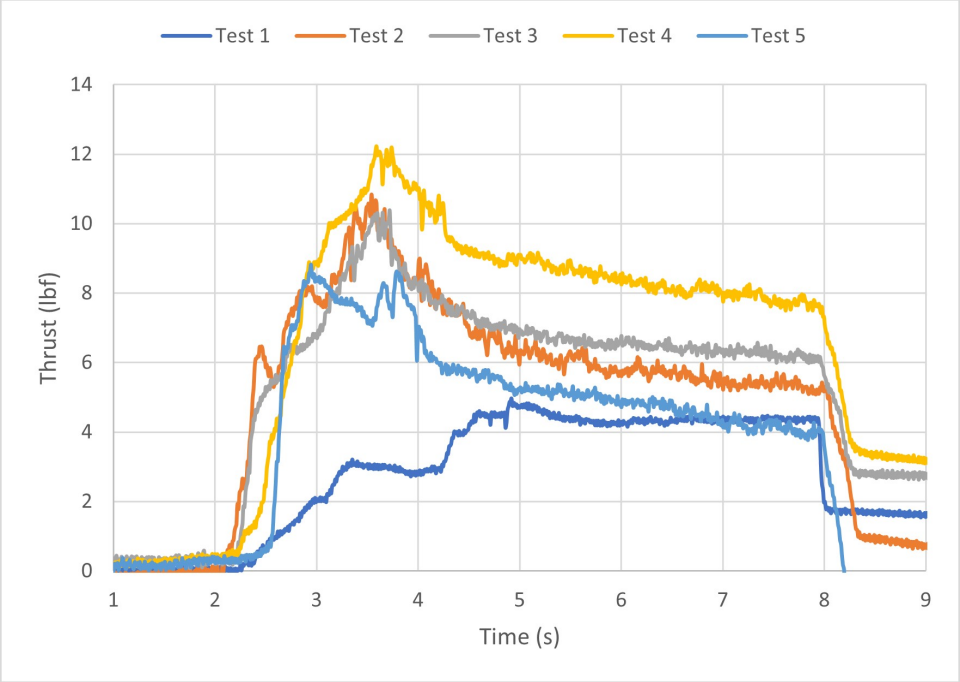

Figure 39: Thrust Versus Time for 50% Infill Density with Triangular Infill Geometry.

4.2.5 50% Infill Density Concentric Infill Geometry

Figure 40 displays the thrust curve profiles against the burn time for the five tests completed with a 50% infill density and a triangular infill geometry. Recall Figure 37 for reference as 50% density with a cubic geometry will be the basis of comparison for infill geometry study. Concentric infill geometry featured burn profiles that were highly variable across the entire burn will multiple local maximums in thrust. The rise time of the 50% concentric fuel grains were all between 2.25 and 2.75 seconds with burns of 5.25 to 5.75 seconds.

Table 14 displays the performance parameters for each hot fire test along with the average and percent standard deviation from all tests of 50% density and concentric geometry. The average and percent standard deviations are calculated based on burn time calculations that result in the start and stop times being based on 10% of the peak thrust value. Although the burn profiles of the concentric geometries were highly variable in nature, the average and percent standard deviations stayed rather low, with the exception being regression rate.

Table 13: Performance Parameter Results for 50% Infill Density with Triangular Infill Geometry.

Test Number	$F_{max}(lbf)$	$\bar{F}(lbf)$	$I(lbf * s)$	$I_{sp}(s)$	$\bar{\dot{r}}(in/s)$
1	4.98	3.68	20.5	115	0.007
2	10.8	6.70	37.4	182	0.013
3	10.4	5.73	33.7	157	0.013
4	12.2	8.36	49.8	238	0.011
5	8.83	5.42	30.6	154	0.011
Average	9.44	5.98	34.4	169	0.011
% Std Dev	29%	29%	31%	27%	21%

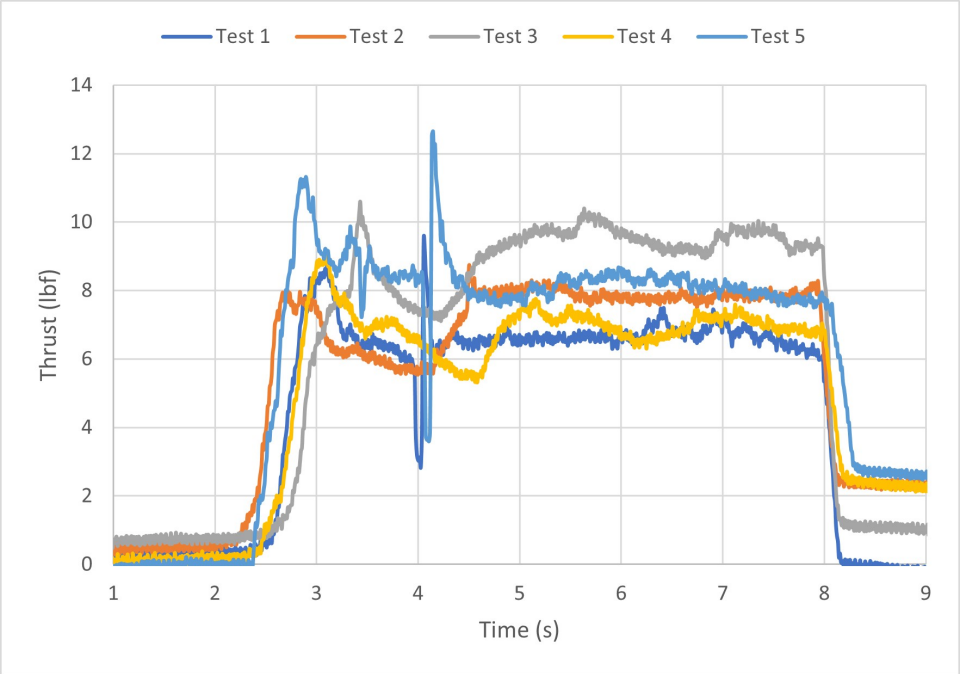

Figure 40: Thrust Versus Time for 50% Infill Density with Concentric Infill Geometry.

4.3 Performance Parameter Results and Analysis

The charts immediately provided serve as an overview of all the tests and how they performed on the measures related to the key performance parameters. It is important to note that

Table 14: Performance Parameter Results for 50% Infill Density with Concentric Infill Geometry.

Test Number	$F_{max}(lbf)$	$\bar{F}(lbf)$	$I(lbf * s)$	$I_{sp}(s)$	$\bar{\dot{r}}(in/s)$
1	9.56	6.45	35.8	180	0.012
2	8.75	7.00	41.6	207	0.009
3	10.6	8.72	48.7	277	0.009
4	9.02	6.56	37.6	194	0.009
5	12.6	7.98	46.7	230	0.011
Average	10.1	7.34	42.1	218	0.010
% Std Dev	16%	13%	13%	17%	21%

different infill densities and infill geometries will cause the system to behave differently. General performance trends regarding each configuration of fuel will be observed.

Hypothesis testing through a series of Analysis of Variance (ANOVA) tests was conducted using a 95% confidence interval for all key performance parameters, with F_{crit} values being tabulated to decide statistical relevance. F_{crit} values being lower than the F value calculated via the ANOVA testing will indicate a statistical significance that can be applied to the data stating that a difference in the means exists. Testing for sample variance was conducted across two separate groups: infill densities and infill geometries. Note that even though some groups may not show statistical relevancy, distinct differences can still be shown to characterize certain groups for future study.

4.3.1 Peak Thrust

Figure 41 shows the average peak thrust value recorded against each separate infill density along with the standard deviations shown as error bars on the graph. Upon observation of the peak thrust values, it appears that there is a deviation from what is expected. The expectation is that they would be inversely proportional. With a lower infill percentage,

there should be more room for oxidizer flow within the infill matrix. This means there is a higher surface area to volume ratio which should incite more burning within the fuel grain. More burning would be indicated with a higher thrust value. The 30% fuel grain exhibiting lower thrust is most likely due to being less structurally sound than the 50% and 70%. The fuel grain infill can not withstand the pressure of the flow in the combustion chamber and is being ejected without experiencing full combustion. The relationship between the 50% and 70% fuel grains are consistent with what is expected from each configuration.

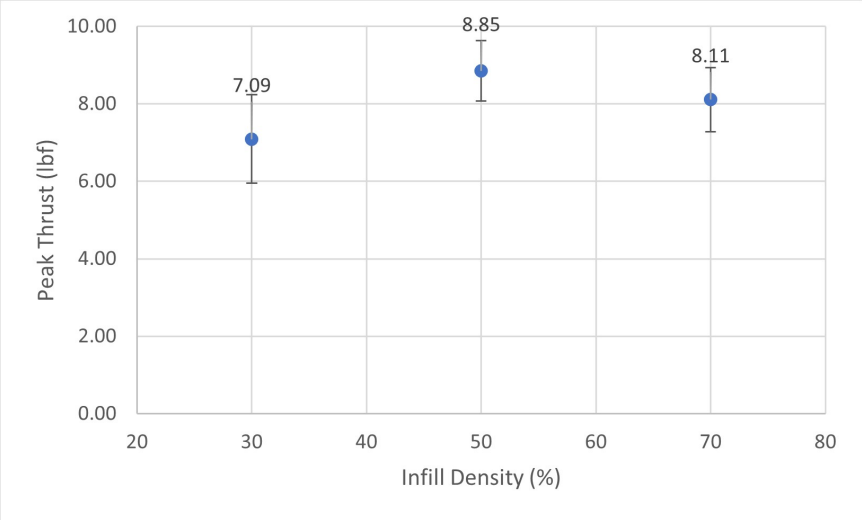

Figure 41: Peak Thrust for Infill Densities of 30%, 50%, and 70%.

Figure 42 shows the average peak thrust value recorded against each separate infill geometry along with the standard deviations shown as error bars on the graph. Results from the infill geometry study show that concentric infill produced the most peak thrust, followed by triangular, then cubic. Please note that while peak thrust is a metric that is used to measure performance of a rocket system, small-scale tests produce highly variable peak thrust values due to igniter size and variance.

Tables 15, 16, 17, and 18 show results from hypothesis testing of fuel grain parameter configuration peak thrust variances. The table shows the group, average, variance, then calculated F and F_{crit} values. By comparing F to F_{crit}, evidence suggests that there is no significant statistical correlation to peak thrust in either study: density or geometry. This

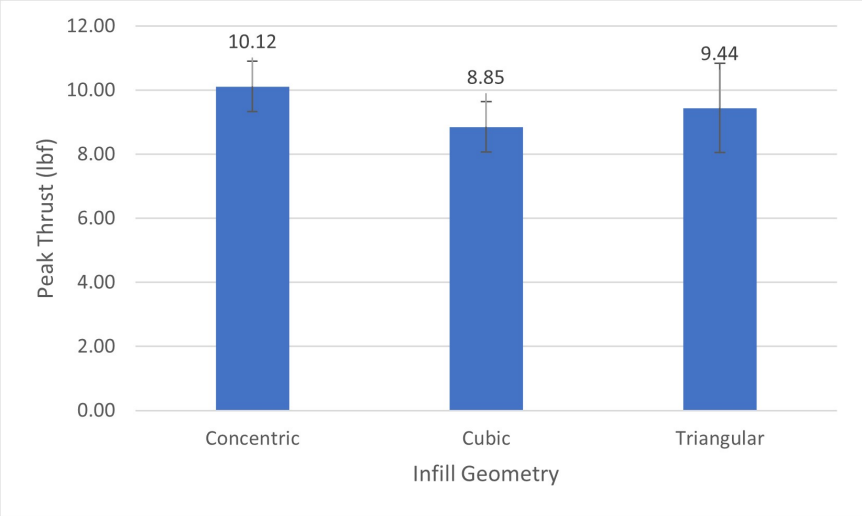

Figure 42: Peak Thrust for Infill Geometries of Concentric, Cubic, and Triangular.

is likely due to the differences in igniters used in this campaign.

Table 15: Peak Thrust Density ANOVA Table Summary.

Group	Average (lbf)	Variance (lbf)
30%	7.09	5.27
50%	8.85	2.45
70%	8.11	2.75

Table 16: Peak Thrust Density ANOVA Results.

F	F_{crit}
1.12	3.88

4.3.2 Average Thrust

Figure 43 shows the average thrust value recorded against each separate infill density along with the standard deviations shown as error bars on the graph. The results obtained from the average thrust comparisons follow that of the peak thrust when comparing differing infill densities. This is likely due to the lack of structural support for the 30% infill, causing incomplete combustion of PLA. The trend of being inversely proportional continues with the 50% and 70% grains.

Table 17: Peak Thrust Geometry ANOVA

Table Summary.

Group	Average (lbf)	Variance (lbf)
Con	10.1	2.51
Cu	8.85	2.45
Tri	9.44	7.73

Table 18: Peak Thrust Geometry ANOVA Results.

F	F_{crit}
0.47	3.88

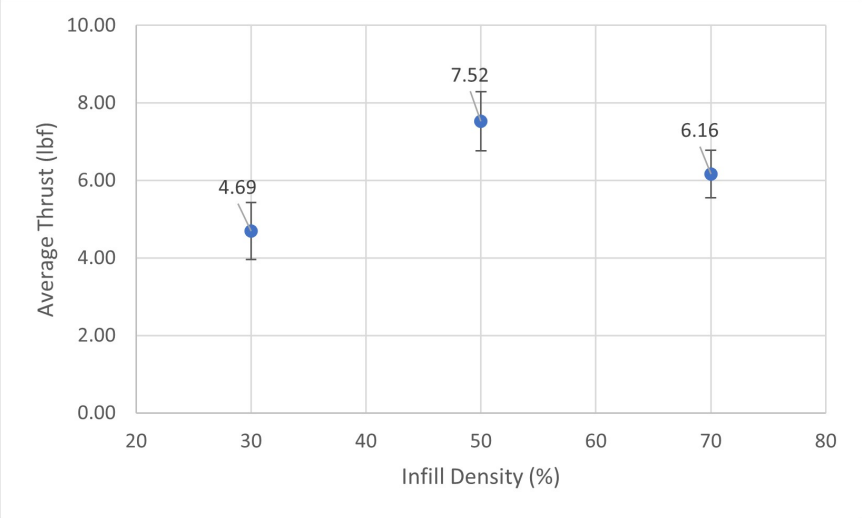

Figure 43: Average Thrust for Infill Densities of 30%, 50%, and 70%.

Figure 44 shows the average peak thrust value recorded against each separate infill geometry along with the standard deviations shown as error bars on the graph. Results from the infill geometry study show that cubic produces the highest overall average thrust. This is likely due to the uniformity in the burn profile associated with the cubic infill geometry. A more complex internal geometry corresponds to a longer time in contact with the infill matrix and more heat transfer to the fuel grain.

Tables 19, 20, 21, and 22 show results from hypothesis testing of fuel grain parameter configuration average thrust variances. The table shows the group, average, variance, then calculated F and F_{crit} values. By comparing F to F_{crit}, evidence suggests that there is a significant statistical correlation to average thrust with regards to infill density due to

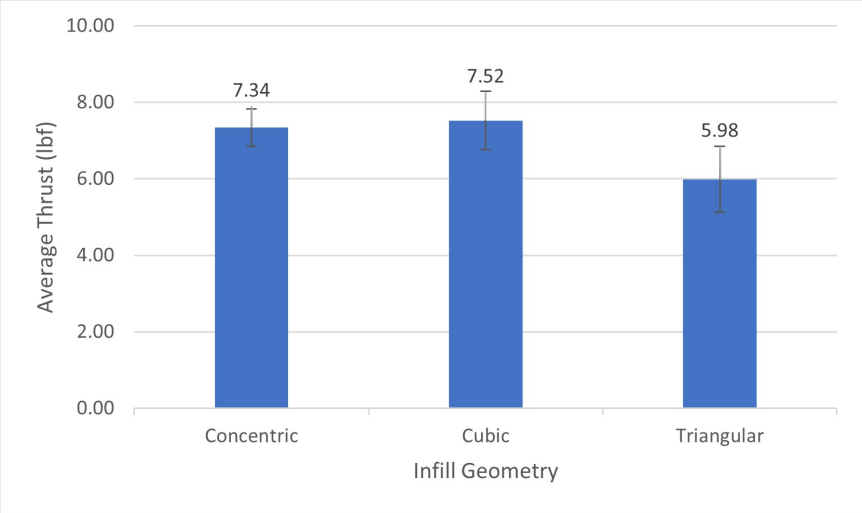

Figure 44: Average Thrust for Infill Geometries of Concentric, Cubic, and Triangular.

the calculated F being greater than F_{crit}. However, there is no statistical significance with regards to the differing infill geometries.

Table 19: Average Thrust Density ANOVA Table Summary.

Group	Average (lbf)	Variance (lbf)
30%	4.69	2.18
50%	7.52	2.31
70%	6.16	1.51

Table 20: Average Thrust Density ANOVA Results.

F	F_{crit}
5.00	3.88

4.3.3 Total Impulse

Figure 45 shows the total impulse value recorded against each separate infill density along with the standard deviations shown as error bars on the graph. The results obtained from the average thrust comparisons follow that of the thrust performance parameters when comparing differing infill densities, as total impulse is directly derived from thrust. This is likely due to the lack of structural support for the 30% infill, causing incomplete combustion of PLA. The trend of being inversely proportional continues with the 50% and 70% grains,

Table 21: Average Thrust Geometry ANOVA Table Summary.

Group	Average (lbf)	Variance (lbf)
Con	7.34	0.96
Cu	7.52	2.31
Tri	5.97	2.97

Table 22: Average Thrust Geometry ANOVA Results.

F	F_{crit}
1.71	3.88

indicating that the 50% infill density produces the most energy over the length of its burn.

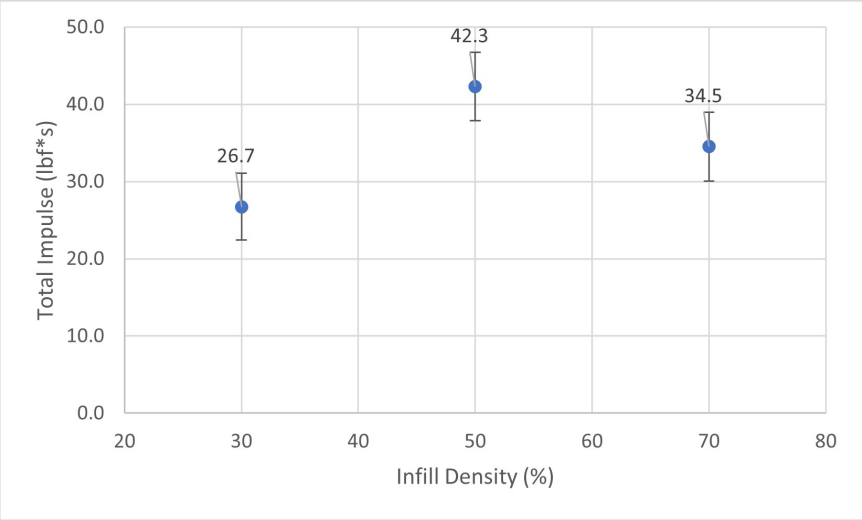

Figure 45: Total Impulse for Infill Densities of 30%, 50%, and 70%.

Figure 46 shows the total impulse value recorded against each separate infill geometry along with the standard deviations shown as error bars on the graph. Results from the infill geometry study show that cubic produces the highest overall total impulse. This indicates that cubic produces the most energy throughout the length of its burn.

Tables 23, 24, 25, and 26 show results from hypothesis testing of fuel grain parameter configuration total impulse variances. The table shows the group, average, variance, then calculated F and F_{crit} values. By comparing F to F_{crit}, evidence suggests that there is a significant statistical correlation to total impulse with regards to infill density due to the calculated F being greater than F_{crit}. However, there is no statistical significance with

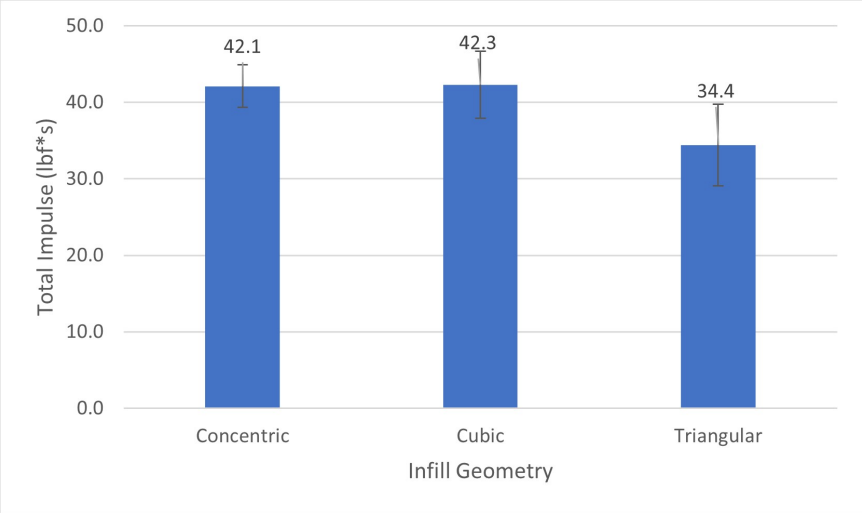

Figure 46: Total Impulse for Infill Geometries of Concentric, Cubic, and Triangular.

regards to the differing infill geometries.

Table 23: Total Impulse Density ANOVA Table Summary.

Group	Average (lbf*s)	Variance (lbf*s)
30%	26.7	74.7
50%	42.3	77.9
70%	34.5	34.5

Table 24: Total Impulse Density ANOVA Results.

F	F_{crit}
3.89	3.88

4.3.4 Specific Impulse

Figure 47 shows the specific impulse value recorded against each separate infill density along with the standard deviations shown as error bars on the graph. The results obtained from the specific impulse comparisons follow that of the total impulse performance parameter when comparing differing infill densities, as specific impulse is directly derived from total impulse. The trend of being inversely proportional continues with the 50% and 70% grains, indicating that the 50% infill density produces the most energy content per unit weight flow over the length of its burn.

Table 25: Total Impulse Geometry ANOVA

Table Summary.

Group	Average (lbf*s)	Variance (lbf*s)
Con	42.1	31.2
Cu	42.3	77.9
Tri	34.4	112.8

Table 26: Total Impulse Geometry ANOVA Results.

F	F_{crit}
1.36	3.88

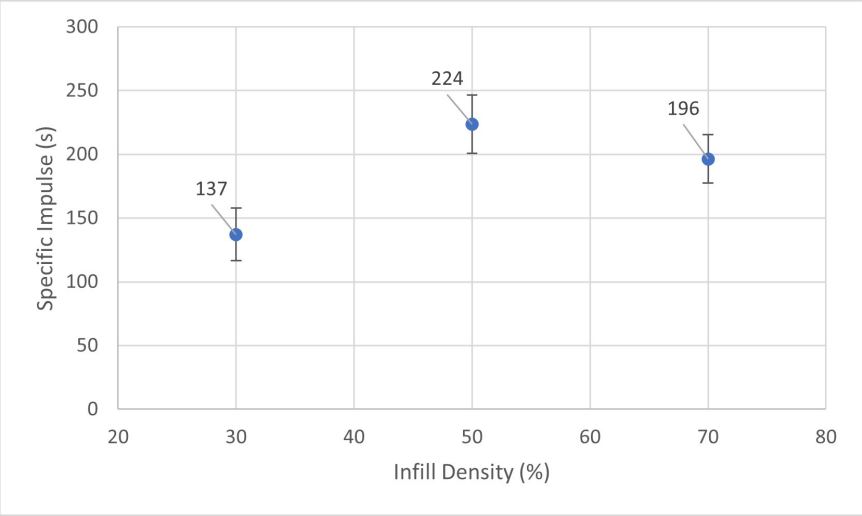

Figure 47: Specific Impulse for Infill Densities of 30%, 50%, and 70%.

Figure 48 shows the specific impulse value recorded against each separate infill geometry along with the standard deviations shown as error bars on the graph. Results from the infill geometry study show that cubic produces the highest overall specific impulse. This indicates that cubic produces the most energy per unit weight flow throughout the length of its burn.

Tables 27, 28, 29, and 30 show results from hypothesis testing of fuel grain parameter configuration specific impulse variances. The table shows the group, average, variance, then calculated F and F_{crit} values. By comparing F to F_{crit}, evidence suggests that there is a significant statistical correlation to specific impulse with regards to infill density due to the calculated F being greater than F_{crit}. However, there is no statistical significance with regards to the differing infill geometries.

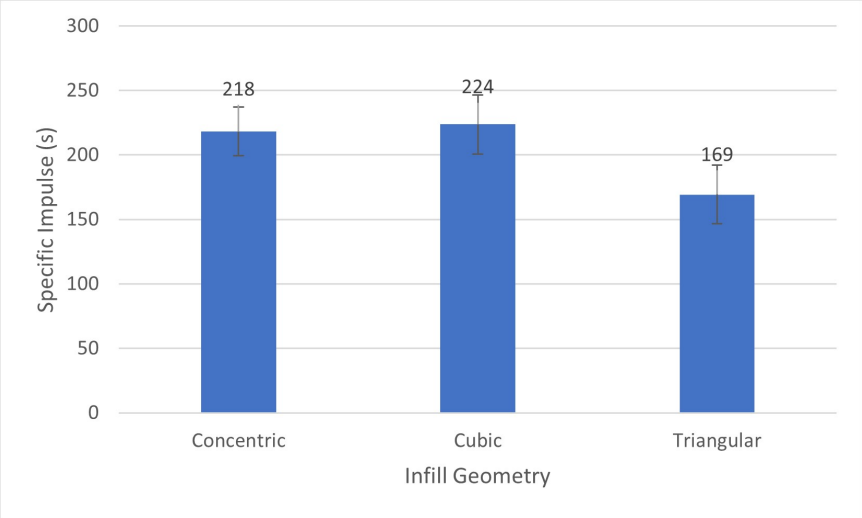

Figure 48: Specific Impulse for Infill Geometries of Concentric, Cubic, and Triangular.

Table 27: Specific Impulse Density ANOVA

Table Summary.

Group	Average (s)	Variance (s)
30%	137	1707
50%	223	2104
70%	198	1272

Table 28: Specific Impulse Density ANOVA Results.

F	F_{crit}
5.83	3.88

4.3.5 Regression Rate

Figure 49 shows the regression rate value recorded against each separate infill density along with the standard deviations shown as error bars on the graph. The results obtained from the regression rate comparisons show an inversely proportional relationship with regression rate and infill density. This indicates that the 30% infill density regresses the most over the length of its burn.

Figure 50 shows the regression rate value recorded against each separate infill geometry along with the standard deviations shown as error bars on the graph. Results from the infill geometry study show that triangular produces the highest overall regression rate. This is likely due to the large peak thrust produced that burns through most of the fuel grain.

Table 29: Specific Impulse Geometry ANOVA Table Summary.

Group	Average (s)	Variance (s)
Con	218	1439
Cu	223	2104
Tri	169	2076

Table 30: Specific Impulse Geometry ANOVA Results.

F	F_{crit}
2.39	3.88

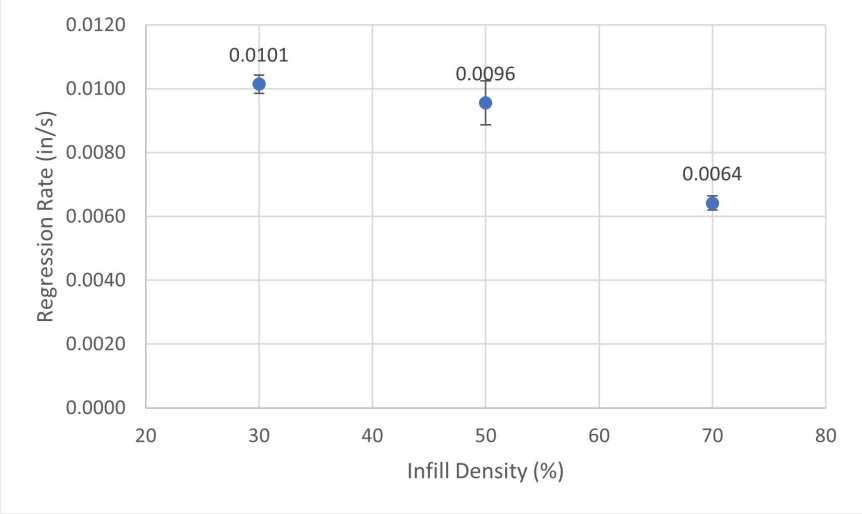

Figure 49: Regression Rate for Infill Densities of 30%, 50%, and 70%.

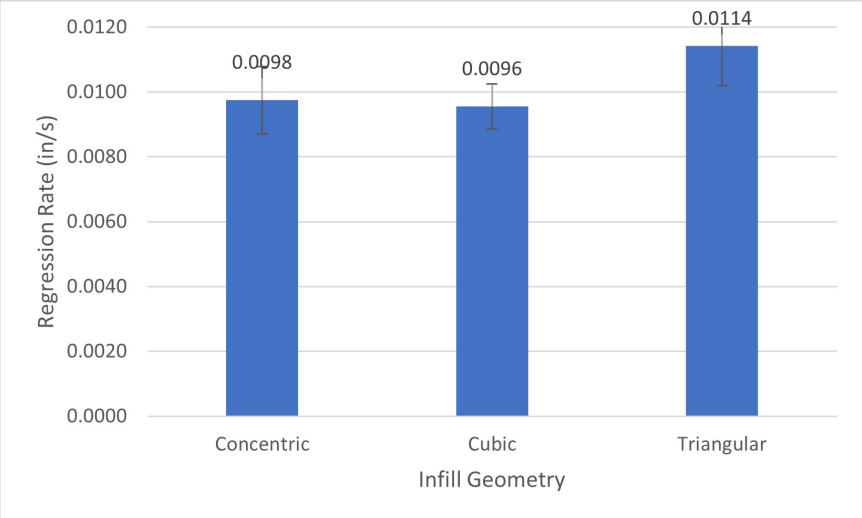

Figure 50: Regression Rate for Infill Geometries of Concentric, Cubic, and Triangular.

Tables 31, 32, 33, and 34 show results from hypothesis testing of fuel grain parameter configuration regression rate variances. The table shows the group, average, variance, then calculated F and F_{crit} values. By comparing F to F_{crit}, evidence suggests that there is a significant statistical correlation to regression rate with regards to infill density due to the calculated F being greater than F_{crit}. However, there is no statistical significance with regards to the differing infill geometries.

Table 31: Regression Rate Density ANOVA Table Summary.

Group	Average (in/s)	Variance (in/s)
30%	0.01	3.32e-7
50%	0.01	1.91e-6
70%	0.006	1.95e-7

Table 32: Regression Rate Density ANOVA Results.

F	F_{crit}
24.7	3.88

Table 33: Regression Rate Geometry ANOVA Table Summary.

Group	Average (in/s)	Variance (in/s)
Con	0.010	4.31e-6
Cu	0.010	1.91-6
Tri	0.011	5.93e-6

Table 34: Regression Rate Geometry ANOVA Results.

F	F_{crit}
1.29	3.88

4.3.6 Ensemble Analysis

In order to observe the consistency of thrust profiles achieved by each fuel density and geometry configuration, an ensemble average was taken for each density and each geometry. Due to the varying nature of the ignition profile, two different ensemble averages will be presented: the rise/ignition phase towards the front of the burn and the steady-state phase

towards the end of the burn. In Figure 51, the ensemble average for thrust profiles of infill density in the ignition period can be viewed, with their error bars representing the thrust standard deviation at each point throughout its burn in that period. Each of the three infill densities exhibit an inversely proportional relationship with the standard deviation, with the percent standard deviations equalling 36%, 25%, and 20% respectively.

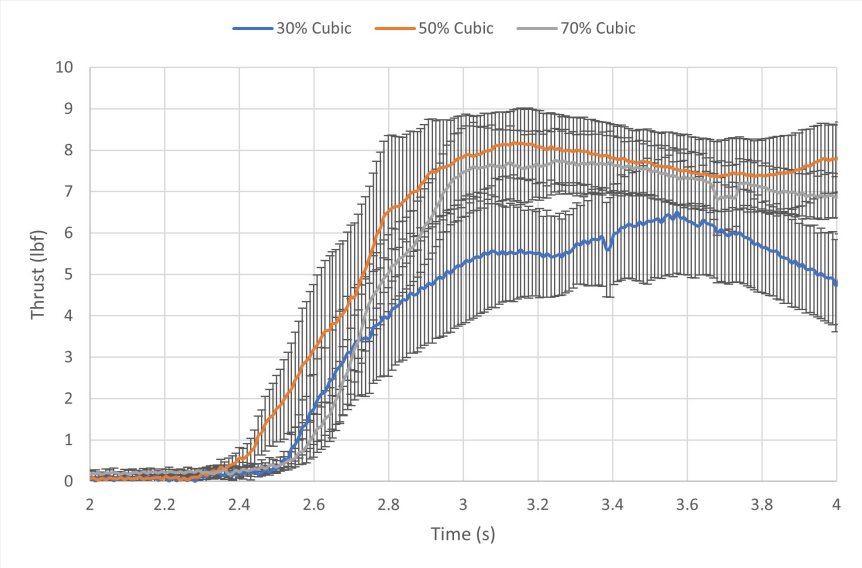

Figure 51: Infill Density Ensemble Average During the Ignition Period.

Figure 52 shows the same thrust profiles in their steady-state period. Here, the ensemble average of the thrust profiles show an even tighter standard deviation of 15%, 22%, and 16% respectively. This drop in standard deviation is likely due to the volatile environment created by the pyrogenic igniters. Once the system has reached steady-state, the nature of the infill density can take affect. The tightness of the 30% infill density is likely due to not having much fuel left to burn towards the end of the steady-state period, which explains its lower value in relation to the other two densities.

Figure 53 displays the average thrust profiles of infill geometries in the ignition period with the error bars representing the thrust standard deviation at each point throughout the burn of that period. The standard deviation from the average thrust for concentric, cubic, and triangular are 26%, 25%, and 37%, respectively. This indicates that cubic geometry

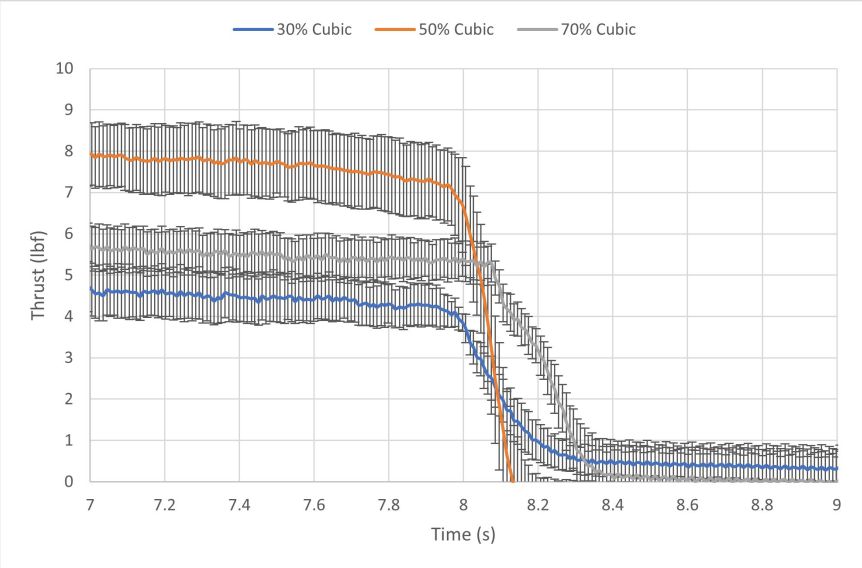

Figure 52: Infill Density Ensemble Average During the Steady-State Period.

experiences the most consistent burn throughout this period. Concentric experiences almost exactly the same standard deviation over this period. Triangular is the most variable throughout the ignition period.

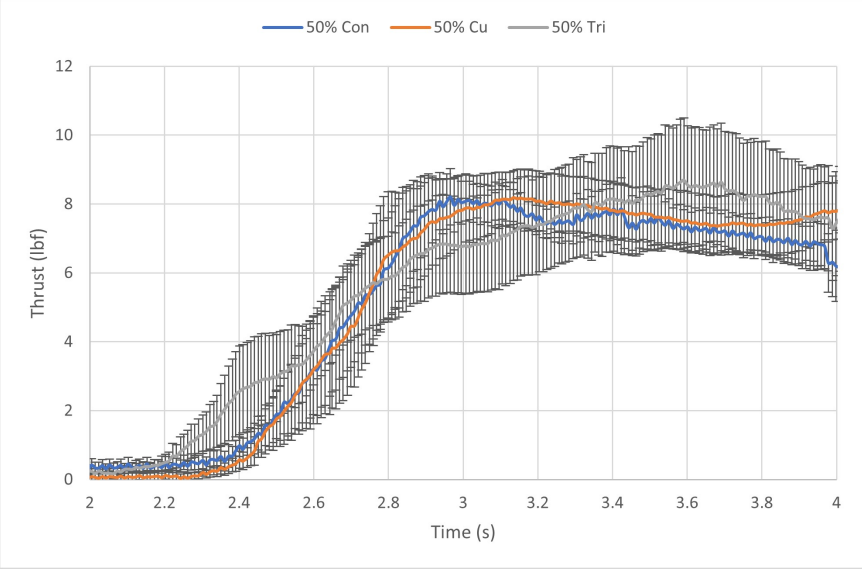

Figure 53: Infill Geometry Ensemble Average During the Ignition Period.

Figure 54 shows the average thrust profiles with respect to infill geometry in their steady-state period. Here, the ensemble average of the thrust profiles of concentric and cubic can

be seen overlapping each other, indicating a very tight similarity in both average value and consistency of burn throughout the steady-state period of their burn profiles. The triangular infill geometry has a lower average value with a higher standard deviation.

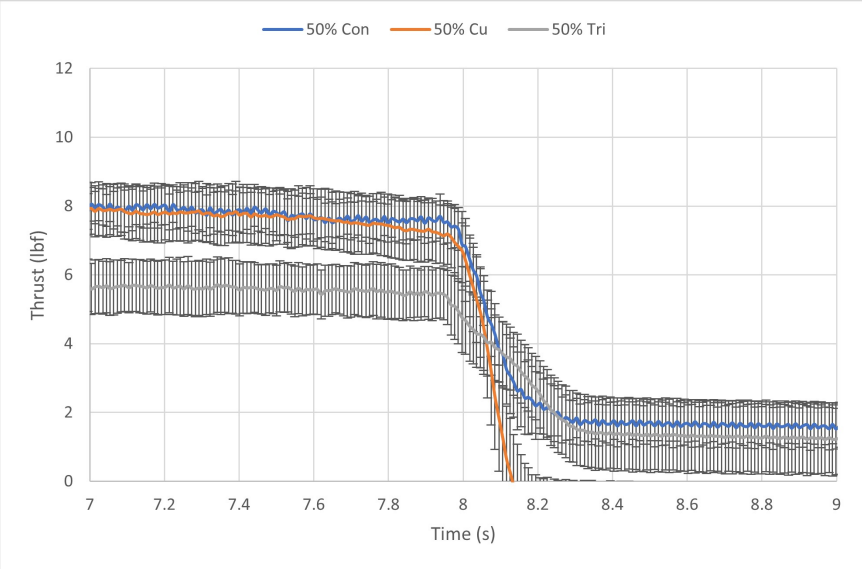

Figure 54: Infill Geometry Ensemble Average During the Steady-State Period.

CHAPTER V

CONCLUSIONS AND RECOMMENDATIONS

5.1 Summary

As mentioned before, the primary goal of this study is to evaluate the differences and consistency of performance relative to changes in infill density and infill geometry, but several performance trends were also observed throughout this study. Average thrust, total impulse, specific impulse, and regression rate all experience an inversely proportional relationship with infill density, with the exception of 30%. The 30% infill density was lackluster in all performance parameters, likely due to its lack of structure as a fuel grain. Its low infill density likely did not provide enough support to withstand the high temperature and pressure of the combustion chamber, and ejected uncombusted PLA out the nozzle. Further studies are needed to fully elaborate on this phenomenon and to determine the minimum infill density for the inversely proportional relationship to take place. These general trends correlate with the findings of other studies such as [12], [22], and [18].

Peak thrust created by the HRE was highly dependent on the igniter used for the test. Around 80% of all peak thrust values came in the ignition phase of the burn profile. Each igniter comes with a small amount of pre-cast solid propellant on the end. With no way to track any variables of that propellant, there is inherent uncertainty in the system.

Although infill geometry had no statistical significance, certain trends were still able to be seen. The concentric infill geometry had a sinusoidal-like thrust curve, indicating periods of high and low thrust. This is likely due to the way concentric prints are printed. Concentric prints are a combination of 100% wall layers followed by a layer of supports. As

heat transferred into the wall layer, it would melt the support layer between the walls. This would weaken the support system and cause periods of high and low thrust based on the layer density. The cubic infill geometry exhibited the most uniform burn profile of the three infill geometries tested. The cubic infill geometry is known for its 3-D strength profile. This makes it an ideal candidate for the use of hybrid rocket fuel. Triangular only exhibits a 2-D strength profile so it would burn out very quickly after spitting out uncombusted PLA like the 30% configuration.

5.1.1 Research Objectives and Outcomes

An analysis on hybrid rocket fuel performance consistency was performed. Several significant and potential significant differences have been attained in infill density. Key outcomes with respect to each objective can be observed in the sections below.

Evaluation of the Infill Density and Geometry on Thrust, Impulse, and Regression Rate

Evaluation of the infill density and geometry on performance and consistency is captured through comparing performance parameter results within the classes of differing infill densities. Beginning with average thrust, 50% infill density were less variable than 30%, with 70% being significantly less variable. This trend carries on for total impulse and specific impulse. When the thrust ensemble averages were observed, minimized deviation from the ensemble average and the highest consistency were achieved in the highest infill density, 70%. The opposite of this trend occurred in the lowest infill density, 30%. These trends vary slightly with regression rate. Both 30% and 70% experience low standard deviations while 50% is less consistent. Differing infill geometries had less of an effect on performance parameters and the ensemble average of the thrust profiles. Concentric and cubic featured almost identical performance parameters across the board. Triangular infill geometry experienced a more variable burn profile in both the ignition and steady-state periods, with higher standard de-

viations among the performance parameters. Small sample hypothesis testing and ensemble profile analysis verify results stated in this section.

5.2 Final Recommendations

Evaluations in performance and consistency relative to variations in infill density show a slight reduction in performance but an increase in consistency as infill density increases. The mission statement determines the need for the configuration of the fuel. More consistent burn profiles may need a higher infill density, while higher performing may want to stay around 50% infill for higher thrust and specific impulse values. A narrowed approach at infill density would further optimize performance to idealize the oxidizer to fuel ratio at play with different infill densities. Scaling effects play a large role in HRE applications. Increasing the diameter and length of the motor casing could provide better insight into the relationships at play between infill density and infill geometry. Although some metrics may be statistically insignificant at a small scale, larger diameter HREs could flesh out those insignificances. Longer casings allow for the use of pre and post combustion chambers, which allow for better oxidizer preheating and mixing before leaving the nozzle. Pre and post combustion chambers produce better optimized systems. Another future parameter to study that can affect performance is the fuel port geometry. Differing areas and shapes can induce turbulence and cause better heat transfer into the fuel grain.

A large design space in the additive manufacturing realm is the build parameters of the printer or slicer. These parameters represent countless fine tuning mechanisms to create more or less consistent prints depending on the type of profile needed for the mission statement. Parameters that can be optimized include print speed, nozzle temperature, bed temperature, and layer thickness. These parameters are specified by the printer and can be easily controlled and modified. To determine their role, further studies must take place by varying these parameters.

Additives to the fuel grain also represent a large design space in the additive manufac-

turing world. There are currently filaments that contain varying amount of metal powders embedded or filling the filament. Fine tuning of these metal powders by weight percentage can have differing effects on the performance parameters discussed in this study. Many metal powders are used as burn rate catalysts in solid rocket motors.

Lastly, different oxidizers and feed pressures can be varied to assess the relationship between combustion and oxidizer to fuel ratio.

REFERENCES

[1] Brian J. Cantwell. *Aircraft and Rocket Propulsion.* AA283 Course Reader. Department of Aeronautics and Astronautics, Stanford University, Stanford, California 94305, July 2022.

[2] Burt Rutan. Spaceshipone. *Encyclopaedia Britannica*, March 2020.

[3] How to use infill percentage and pattern – enhance strength, save material. *Tianse Office*, 2019.

[4] Jack D Mattingly and Keith Boyer. *Elements of propulsion.* AIAA Education Series. American Institute of Aeronautics & Astronautics, Reston, VA, 2 edition, September 2016.

[5] Stephen D Heister, William E Anderson, Timothee L Pourpoint, and R Joseph Cassady. *Rocket Propulsion.* Cambridge Aerospace Series. Cambridge University Press, Cambridge, England, February 2019.

[6] George P Sutton and Oscar Biblarz. *Rocket Propulsion Elements.* John Wiley & Sons, Nashville, TN, 9 edition, December 2016.

[7] Dario Pastrone. Approaches to low fuel regression rate in hybrid rocket engines. *Int. J. Aerosp. Eng.*, 2012:1–12, 2012.

[8] G Marxman and M Gilbert. Turbulent boundary layer combustion in the hybrid rocket. *Symp. Int. Combust.*, 9(1):371–383, January 1963.

[9] G A Marxman, C E Wooldridge, and R J Muzzy. Fundamentals of hybrid boundary-layer combustion. In *Heterogeneous Combustion*, Progress in astronautics and aeronautics, pages 485–522. Elsevier, 1964.

[10] Gerald A Marxman. Combustion in the turbulent boundary layer on a vaporizing surface. *Symp. Int. Combust.*, 10(1):1337–1349, January 1965.

[11] George E Moore and Kurt Berman. A solid-liquid rocket propellant system. *J. Jet Propuls.*, 26(11):965–968, November 1956.

[12] Stephen A Whitmore, Sean D Walker, Daniel P Merkley, and Mansour Sobbi. High regression rate hybrid rocket fuel grains with helical port structures. *J. Propuls. Power*, 31(6):1727–1738, November 2015.

[13] David Altman. Hybrid rocket development history. In *27th Joint Propulsion Conference*, Reston, Virigina, June 1991. American Institute of Aeronautics and Astronautics.

[14] Jason B. publisher = Jones. Am basics.

[15] Thi Nga Tran, Ilker S Bayer, José Alejandro Heredia-Guerrero, Michela Frugone, Marco Lagomarsino, Fabio Maggio, and Athanassia Athanassiou. Cocoa shell waste biofilaments for 3D printing applications. *Macromol. Mater. Eng.*, 302(11):1700219, November 2017.

[16] Scott Landes and Todd Letcher. Mechanical strength of bamboo filled PLA composite material in fused filament fabrication. *J. Compos. Sci.*, 4(4):159, October 2020.

[17] Valentina Mazzanti, Lorenzo Malagutti, and Francesco Mollica. FDM 3D printing of polymers containing natural fillers: A review of their mechanical properties. *Polymers (Basel)*, 11(7):1094, June 2019.

[18] Mitchell McFarland and Elsa Antunes. Small-scale static fire tests of 3d printing hybrid rocket fuel grains produced from different materials. *Aerospace*, 6(7), 2019.

[19] Stephen Whitmore, Zachary Peterson, and Shannon Eilers. Analytical and experimental comparisons of HTPB and ABS as hybrid rocket fuels. In *47th AIAA/ASME/SAE/ASEE Joint Propulsion Conference & Exhibit*, Reston, Virigina, July 2011. American Institute of Aeronautics and Astronautics.

[20] Donald Garlotta. A literature review of poly(lactic acid). *Journal of Polymers and the Environment*, 9(2):63–84, 2002.

[21] David L Kaplan, editor. *Biopolymers from renewable resources*. Macromolecular Systems - Materials Approach. Springer, Berlin, Germany, December 2010.

[22] Byeonguk Ahn, Jeongmoo Huh, Vikas Khandu Bhosale, and Sejin Kwon. Three-dimensionally printed polylactic acid as solid fuel for hydrogen peroxide hybrid rockets. *J. Propuls. Power*, 37(1):171–175, January 2021.

[23] Joseph V Rutkowski and Barbara C Levin. Acrylonitrile-butadiene-styrene copolymers (ABS): Pyrolysis and combustion products and their toxicity?a review of the literature. *Fire Mater.*, 10(3-4):93–105, September 1986.

[24] Szymon Wojtyła, Piotr Klama, and Tomasz Baran. Is 3D printing safe? analysis of the thermal treatment of thermoplastics: ABS, PLA, PET, and nylon. *J. Occup. Environ. Hyg.*, 14(6):D80–D85, June 2017.

[25] Yuna Kim, Chungsik Yoon, Seunghon Ham, Jihoon Park, Songha Kim, Ohhun Kwon, and Perng-Jy Tsai. Emissions of nanoparticles and gaseous material from 3D printer operation. *Environ. Sci. Technol.*, 49(20):12044–12053, October 2015.

[26] John R. Hart. Chemical equilibrium and molar group contribution analysis of the flammability of poly-3-hydroxybutyrate. *Polymer Degradation and Stability*, 98(1):387–391, 2013.

[27] Hongmei Chen, Fengyi Chen, Hui Chen, Hongsheng Liu, Ling Chen, and Long Yu. Thermal degradation and combustion properties of most popular synthetic biodegradable polymers. *Waste Manag. Res.*, 41(2):431–441, February 2023.

[28] John Campbell, Frank Macklin, and Zachary Thicksten. Handling considerations of nitrous oxide in hybrid rocket motor testing. In *44th AIAA/ASME/SAE/ASEE Joint Propulsion Conference & Exhibit*, Reston, Virigina, July 2008. American Institute of Aeronautics and Astronautics.

[29] C Carmicino and A Russo Sorge. Experimental investigation into the effect of solid-fuel additives on hybrid rocket performance. *J. Propuls. Power*, 31(2):699–713, March 2015.

[30] Alec William Yenawine. Hybrid rocket engines: Development of composite fuels with complex 3d printed ports. *University of Miami Master of Science Thesis*, 2019.

[31] Kevin Lohner, Jonny Dyer, Eric Doran, Zachary Dunn, and Greg Zilliac. Fuel regression rate characterization using a laboratory scale nitrous oxide hybrid propulsion system. In *42nd AIAA/ASME/SAE/ASEE Joint Propulsion Conference & Exhibit*, Reston, Virigina, July 2006. American Institute of Aeronautics and Astronautics.

[32] Xiaodong Yu, Hongsheng Yu, Wei Zhang, Luigi T DeLuca, and Ruiqi Shen. Effect of penetrative combustion on regression rate of 3D printed hybrid rocket fuel. *Aerospace*, 9(11):696, November 2022.

[33] Jeff Smith. Ask away: Optimizing your nitrous system with proper bottle pressure, Jul 2022.

APPENDICES

HRE Test Results

Table 35: HRE Test Results

Test Number	$F_{max}(lbf)$	$\bar{F}(lbf)$	$I(lbf * s)$	$I_{sp}(s)$	$\bar{\dot{r}}(in/s)$
1.30cu	7.46	4.99	30.2	145	0.010
2.30cu	8.00	4.43	24.9	130	0.010
3.30cu	10.3	7.07	39.9	204	0.011
4.30cu	4.74	3.51	19.8	104	0.010
5.30cu	4.99	3.46	18.9	103	0.010
1.50cu	10.63	9.50	54.8	288	0.008
2.50cu	6.82	5.41	30.7	160	0.009
3.50cu	8.24	7.27	39.9	222	0.008
4.50cu	10.22	8.34	45.5	236	0.011
5.50cu	8.36	7.09	40.5	211	0.009
1.70cu	6.72	5.64	32.2	181	0.006
2.70cu	7.73	5.59	33.3	179	0.006
3.70cu	6.52	4.69	21.35	159	0.006
4.70cu	9.16	7.44	43.6	238	0.006
5.70cu	10.4	7.45	42.1	233	0.007

Test Number	$F_{max}(lbf)$	$\bar{F}(lbf)$	$I(lbf * s)$	$I_{sp}(s)$	$\bar{\dot{r}}(in/s)$
1.50tri	4.98	3.68	20.5	115	0.007
2.50tri	10.8	6.70	37.4	182	0.013
3.50tri	10.4	5.73	33.7	157	0.013
4.50tri	12.2	8.36	49.8	238	0.011
5.50tri	8.83	5.42	30.6	154	0.011
1.50con	9.56	6.45	35.8	180	0.012
2.50con	8.75	7.00	41.6	207	0.009
3.50con	10.6	8.72	48.7	277	0.009
4.50con	9.02	6.56	37.6	194	0.009
5.50con	12.6	7.98	46.7	230	0.011

VITA

Zackery James Bycko

Candidate for the Degree of

Master of Science

Thesis: EFFECT OF ADDITIVE-MANUFACTURED FUEL GRAIN GEOMETRY ON SMALL-SCALE HYBRID ROCKET PERFORMANCE

Major Field: Mechanical and Aerospace Engineering

Biographical:

Education:

Completed the requirements for the Master of Science in Mechanical and Aerospace Engineering at Oklahoma State University, Stillwater, Oklahoma in May, 2023.

Completed the requirements for the Bachelor of Science in Mechanical Engineering at Oklahoma State University, Stillwater, Oklahoma in 2021.

Completed the requirements for the Bachelor of Science in Aerospace Engineering at Oklahoma State University, Stillwater, Oklahoma in 2021.

Professional Memberships:

American Institute of Astronautics and Aeronautics